Himalayan strain reservoir inferred from limited afterslip following the Gorkha earthquake

Electronic supplement: The supplement consists of the full acknowledgements, detailed methods and an appendix of the 28 GPS post-seismic time series from which afterslip following the earthquake was calculated. The time series for each of these GPS sites is tabulated.

Acknowledgements

Methods

1. Geodetic Observations and displacement calculations

GPS data collected in Nepal were obtained from the UNAVCO archive and from the California Institute of Technology (all data used in this study are available at the UNAVCO archive). Data are processed with GOA 6.2 [9,33] using non-fiducial orbits and transformed into the IGS08 frame with orbit, clock and Xfile products obtained from JPL version 2.1. Tropospheric corrections were made with the VMF products from the Vienna University of Technology [27] and Ocean loading corrections were obtained from the Onsala Space Observatory . The India frame used in this study is defined by holding the IGS cGPS stations IISC, BAN2 and HYDE fixed and using the GCCM software developed and used for MORVEL[18,19]. We estimate angular velocities and India fixed velocities using methods described by DeMets et al. (1990) and fitting functions from Ward (1990) and Bos et al. (2013). For sites that have pre-earthquake data, inter-seismic velocities and offsets for the April 25th, 2015 M7.8 Ghorka event were obtained using MLE methods [13]. For those stations that do not have pre-earthquake data, inter-seismic velocities were estimated using the methods outlined in Savage (1983)
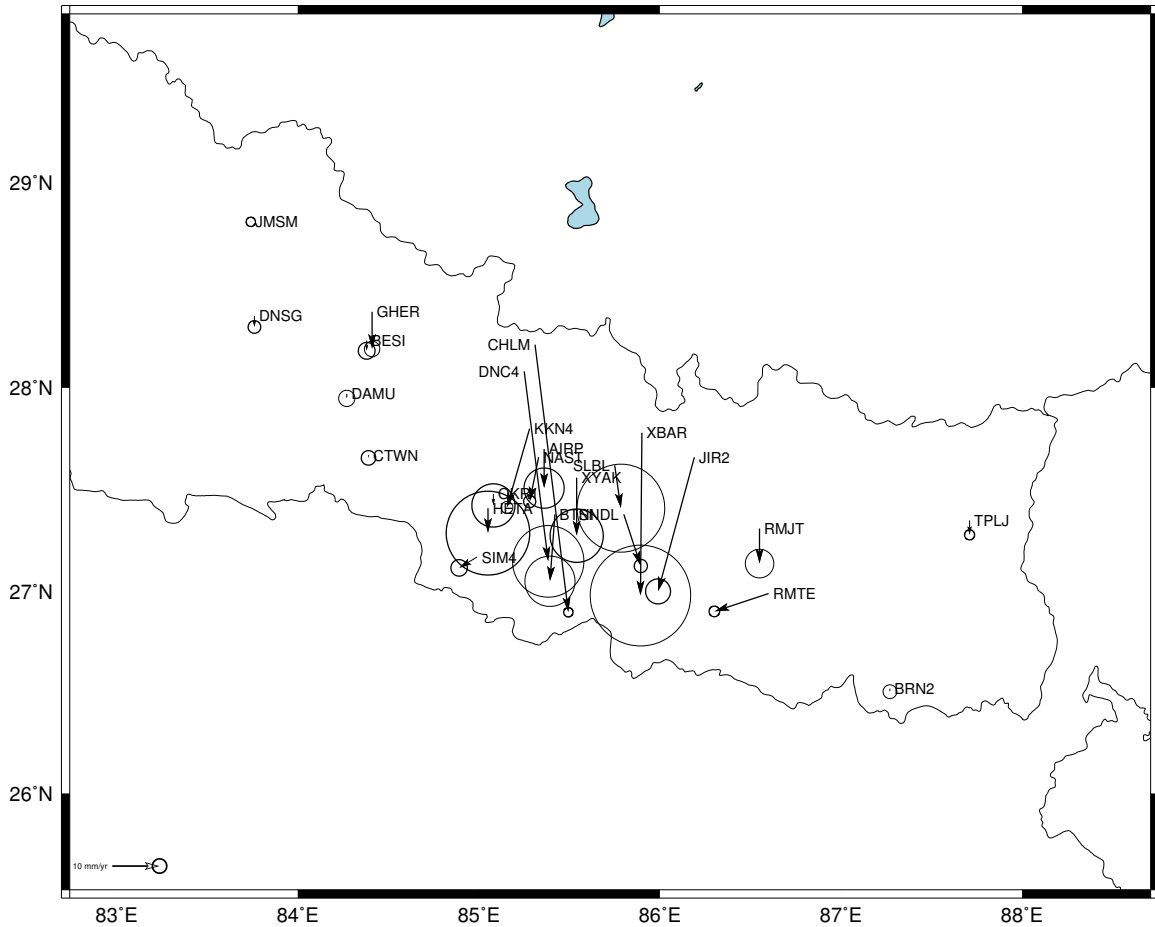
Figure M1. Map showing calculated post-seismic displacements with $\tau = 43$ at 180 days' post-earthquake. (Value A_{43} in Table M1). At all sites except RMTE, the east component is ≤5% of the total magnitude, but doubles the uncertainty of the resultant vector due to large errors in the seasonal signal. In forward models we use the north component. Sites used are shown in Figure 1 in the main text
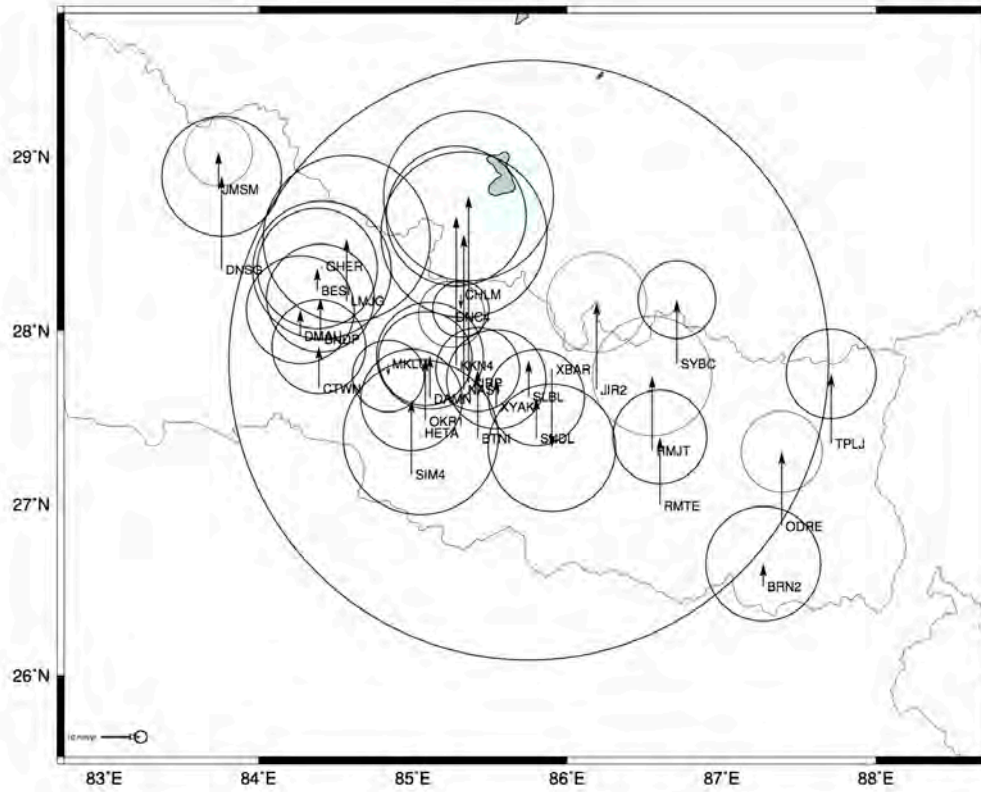
2

Figure M2. Map showing calculated vertical post-seismic displacements with $\tau = 43$ at 180 days' post-earthquake. Vertical uncertainties in processed position and the appropriate correction for monsoon loading (the time period is too short using GRACE data so GLDAS data is used) result in large errors, and we do not use vertical constraints in forward models.

Table M1. Interseismic India-fixed velocities and afterslip decay rates for continuous GPS sites. Column headers are described below the table.

site	east	north	N_{MFT}	N_{dir}	V_N	V_E	A_{180}	Std_{180}	A_{43}	Std_{43}
AIRP	85.36	27.7	66	54	-3.98	-8.53	8.24	2.80	5.7	1.9
BESI	84.38	28.23	79	105	-5.37	-11.51	2.17	1.17	1.9	1.0
BNDP[a]	84.4	27.95	51	71	-2.36	-5.05	-	-	-	-
BRN2	87.27	26.52	29	-27	-1.21	-2.6	0.64	0.96	0.6	0.9
BTNI	85.42	27.38	36	23	-1.45	-3.11	14.14	3.50	4.6	1.2
CHLM	85.31	28.21	95	108	-0.47	-9.72	56.46	0.65	55.4	0.6
CTWN	84.39	27.67	23	39	-1.0	-2.16	0.58	1.01	0.5	0.9
DAMN	85.11	27.61	46	37	-2	-4.28	5.2	6.7	4.0	5.2
DMAU	84.27	27.97	63	75	-2.1	-4.49	0.96	1.13	0.9	1.1
DNC4	85.25	28.08	99	87	-6.56	-14.07	40.07	4.98	10.9	1.4
DNSG	83.76	28.35	66	77	-0.84	-8.22	2.33	0.88	2.3	0.9
GHER	84.41	28.37	94	110	-6.35	-13.61	7.83	1.08	7.7	1.1
GUMB[b]	87.86	27.91	90	91	-	-	-	-	-	-
HETA	85.05	27.41	24	16	-1.04	-2.23	5.26	5.83	1.8	2.0
JIR2	86.19	27.66	97	73	-6.47	-13.89	28.28	1.74	14.1	0.9
JMSM	83.74	28.81	111	127	-6.87	-14.74	0.13	0.65	0.1	0.6
KKN4	85.28	27.8	73	62	-0.96	-4.31	16.61	0.83	16.3	0.8
LMJG	84.57	28.17	80	95	-5.52	-11.84	0.71	1.61	0.7	1.6
MKLU	84.84	27.81	55	54	-2.74	-5.87	2.1	5.2	0.8	2.0
NAST	85.33	27.66	61	49	-3.33	-7.15	9.35	0.85	9.2	0.8
ODRE	87.39	26.87	69	16	0.59	-1.64	3.1	4.9	1.9	3.0
OKR1	85.08	27.48	32	23	-1.29	-2.76	2.44	3.01	1.6	1.9
RMJT	86.55	27.31	77	52	-1.96	-6.15	7.38	1.99	4.0	1.1
RMTE	86.6	26.99	47	25	-2.13	-2.86	3.79	0.74	3.7	0.7
SIM4	84.99	27.17	-3	-13	-0.6	-1.3	2.30	1.15	1.8	0.9
SLBL	85.75	27.62	74	57	-4.96	-10.64	9.02	6.12	4.0	2.7
SNDL	85.8	27.38	52	36	-1.01	-3.77	10.90	0.92	10.7	0.9
SYBC	86.71	27.81	134	111	-1.38	-11.47	30.7	1.5	30.5	1.5
TPLJ	87.71	27.35	131	70	-7.2	-15.43	3.05	0.70	3.0	0.7
XBAR	85.9	27.78	97	78	-6.46	-13.86	34.33	7.01	9.2	1.9
XYAK	85.54	27.56	59	46	-3.19	-6.85	12.23	3.71	3.5	1.1

(a): No plausible fit was possible (b): No GLDAS correction available at time of publication

Units and column notation adopted in Table 1:

Site is the four character site name in the UNAVCO archive. Coordinates in degrees.

N_{MFT} perpendicular distance (km) from simplified location for MFT in Figure S3 below.

N_{dir} distance in km to closest mapped most southerly expression of MFT

V_N north interseismic velocity (mm/yr) in an India fixed frame. With the exception of sites listed in Table S2 these velocities are calculated usng a backslip calculation based on distance from the interseismic locking line using N_{MFT}

V_E east interseismic velocity (mm/yr) in an India fixed frame.

A_{180} is the total surface afterslip displacement in mm for the 6 months after the mainshock

std $_{180}$ is the one sigma standard deviation calculated for A_{180} in mm.

A_{43} is the exponential decay constant (mm) evaluated using the expression

$y_0 = A_{43} \exp\{-(x-x_0)/43)\}$
where y_0 is the N component of the surface displacement since the mainshock.
Std$_{43}$ is the standard deviation derived for A_{43} with $\boldsymbol{\tau}$ = 43 days* .

*Calculation of mean decay rate. We first detrended the post seismic data using a mean seasonal value derived from several years of pre-seismic data, and fit a synthetic exponential decay curve to the residuals to derive the following values for $\boldsymbol{\tau}$ (tau1) and variance (σ1). However, the inter-annual variability caused by variable monsoon loading is significant and the application of an empirical correction was deemed insufficient. Accordingly, to more precisely correct for monsoon loading we calculated the seasonal load based on the convolution of hydrological loading data from GLDAS data and a gravitating, layered, spherical earth model (Farrell, 1972). This yielded a much reduced $\boldsymbol{\tau}$ (Tau2) with a reduced variance (σ2) as indicated in Table M2.

Table M2. Least squares fits to decay time-constant with (Tau2± σ2) and without (Tau1 ± σ1) correction for monsoon loading.

site	Tau1, days	$\sigma1$	Tau2, days	$\sigma2$
CHLM	55.774	2.37	47.311	2
DNC4	53.828	31.8	30.45	17.3
KKN4	39.512	5.04	29.081	3.77
NAST	79.571	27.6	56.752	21.8
MEAN	53	5	43	2

The weighted variance in Table M2 is calculated as follows. The variance in each tau is defined as:

$$\omega_i = \frac{1}{\sigma_i^2}$$

with the weighted mean defined as follows:

$$\bar{x} = \frac{\sum_{i=1}^{n}(x_i \sigma_i^{-2})}{\sum_{i=1}^{n} \sigma_i^{-2}}$$

which leads to weighted variance:

$$\sigma_{\bar{x}}^2 = \frac{1}{\sum_{i=1}^{n} \sigma_i^{-2}}$$

This resulting weighted $\boldsymbol{\tau}$, Tau2 = 43±2 days, was applied to all the data with the assumption that variations of the observed afterslip process are unlikely to occur over the spatial scales considered. For the four test sites the change in A_{180} caused by assuming uniform Tau=43 days is insignificant. For those sites which were started days or weeks after the mainshock and the calculation of Tau was problematic, the availability of a reliable Tau provides a crucial constraint to estimate afterslip-induced displacements that occurred prior to installation.
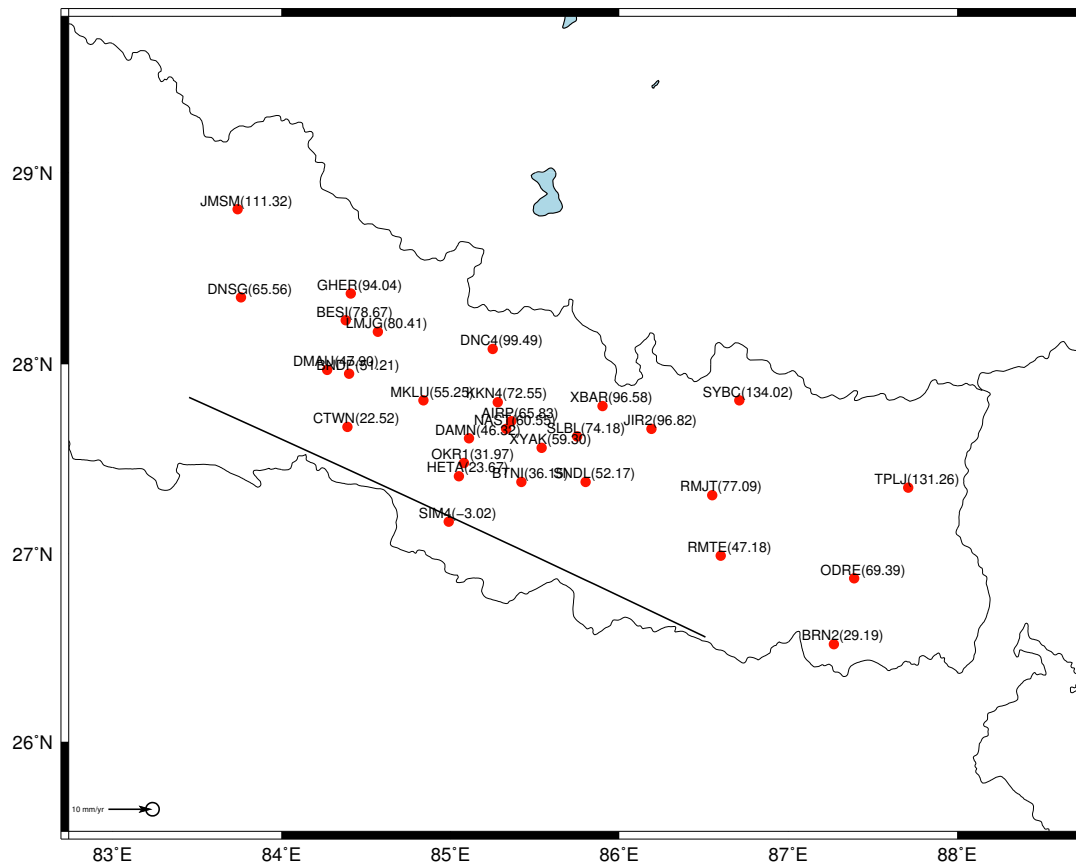
Figure M3. Map showing line selected for approximating the location of the Main Frontal Fault (MFT) used to calculate interseismic velocity corrections for sites for which no pre-seismic data were available, and to compare with deformation modeling described in Section 2. Time series for each of the sites are paginated in the electronic supplement.

2. Numerical Simulations

The simulations solve the coupled time-dependent equations for deformation in a viscoelastic continuum with conservation of mass using a generalized Maxwell model: $\tau_v = \frac{\eta_v}{G}$, $\sigma_q = 2G_v\big(\varepsilon_{el,dev} - \varepsilon_v\big)$, and $\tau_v\dot{\varepsilon}_v + \varepsilon_v = \varepsilon_{el,dev}$ where τ_v is the relaxation time of the viscous element, η_v is the viscosity of the viscous element, and G is the shear modulus. The sum of the stresses in the viscoelastic branches is $\sigma_q = \sum_{m=1}^{N} 2G_m \left(\varepsilon - \gamma_m\right)$ and the total stress is $\sigma = \sigma_0 + C : \varepsilon_{el} + \sigma_q$ using the usual convention where σ is stress, ε strain, with the subscript *el* denoting the elastic component, *dev* the deviatoric component, and *v* the volumetric component. The PDEs are solved on a finite element mesh with variable node spacing to provide the highest resolution around the fault discontinuity, especially in the portions with

6

higher geometric complexity. The time steps are adaptively selected to maintain solution stability, resulting in very small time steps (sometimes seconds) early in the immediate postseismic interval after rupture and then larger later. Solutions for displacement, strain, instantaneous velocity and stress for each node in the meshed domain are stored at intervals of 10 days for comparison to the observed surface displacement time series. The total displacement of each node for a given interval can also be tracked for comparison to the total observed displacement from each GPS installation. All calculations are done in the commercial finite element computing environment of COMSOL 5.2 (www.comsol.com) using the structural mechanics module.

The material conditions include a 20 or 25 km thick elastic lid (so no viscous element, reducing the continuum formulation to Hook's Law) over the generalized Maxwell viscoelastic half space, with initial stresses arising from the coseismic slip distribution. For all simulations, the upper surface boundary condition is free, the basal boundary condition is symmetric (hence approximates a half-space), and the edge conditions far from the rupture area are fixed. The condition on the brittle-ductile interface is one of strict displacement continuity. Also for all simulations, the geometry of the main fault hosting the coseismic rupture is planar, dipping at 7° (6,8), with the rupture epicenter at 15 km depth (4,6,8), and with the coseismic slip distribution given by a joint inversion of InSAR and teleseismic P waveforms (1,2,7) including the 12 May aftershock. This coseismic displacement field, applied to the fault interface, is used to calculate a static stress change used as the initial condition for the time-dependent generalized Maxwell solution described above. The interface between the elastic and viscoelastic domains is set at 25 km depth in the preferred solutions, based on estimates of the maximum depth of seismic rupture (1,2,7). We adopt the ramp-flat-ramp-flat geometry of the Main Himalayan Thrust published by Elliot et al. (2015) converted to our model coordinate system where x=0, y=0 corresponds to the mainshock epicenter, the strike direction is the y-axis, and the dip direction the x-axis.

Model runs for a range of fault frictional conditions on each fault plane geometric segment were initially compared to model runs where the same patches were either fixed (locked) or freely slipping (roller) (Figure M4). We found that, because of the relatively simple material model, the surface displacements predicted for frictional or bounding surface conditions were identical, and differed only in the magnitude of stress dissipation on the interface, with the locked/free slip conditions less dissipative, so providing an upper bound on the fault surface stress after the simulation time interval. To reduce computation run times and improve solution stability, we therefore proceeded to explore the full range of fault surface conditions using the locked/free slip conditions rather than estimating coefficients of friction on fault patches without observational constraints. We tested the range of fault patch models for material models with a range of thicknesses for the elastic lid (15-30 km thick in 5 km steps) and a range of viscosities for the half space from 10^{17}-10^{22} Pa s. The preferred elastic lid thickness is 25 km, based on *a priori* information about the maximum rupture depth and, secondarily, the length scaling of observed surface coseismic displacement.   We could not select a preferred viscosity based on the observed postseismic interval, because all of the tested viscosities showed the same response for the first 6 months of postseismic deformation. Only viscosities much less than our lowest tested value would be expected to show measureable flow in 6 months, and those viscosities are inconsistent with our current understanding of realistic properties for earth materials. Therefore, we chose a viscosity of 10^{19} Pa s for the preferred model. Longer observational epochs currently being collected will eventually provide better constraints on the viscosity term. The lack of postseismic relaxation in the model volume requires the critical conclusion that most, if not all, of the observed surface displacement in the immediate postseismic interval must be attributed to afterslip on the fault plane and the elastic response of the volume.

Finally, the calculated surface displacement magnitudes and full horizontal vector displacements were compared to the observed surface displacements, in order to identify the preferred simulation with respect the the spatial distribution of afterslip on the fault interface. Surface displacement solutions for models with free afterslip on the whole fault interface give surface displacements with very large magnitudes and often the wrong sign (Figure M5). Solutions with more patches of free slip overestimate the surface displacements (Figure M6). The best-fitting numerical solution restricts planar afterslip to the region downdip of the coseismic patch and below the deep ramp on the fault surface. It also allows diffuse deformation below the brittle-ductile transition (BDT), resulting in deflection of the BDT surface and a related diffuse surface displacement (Figure M7).
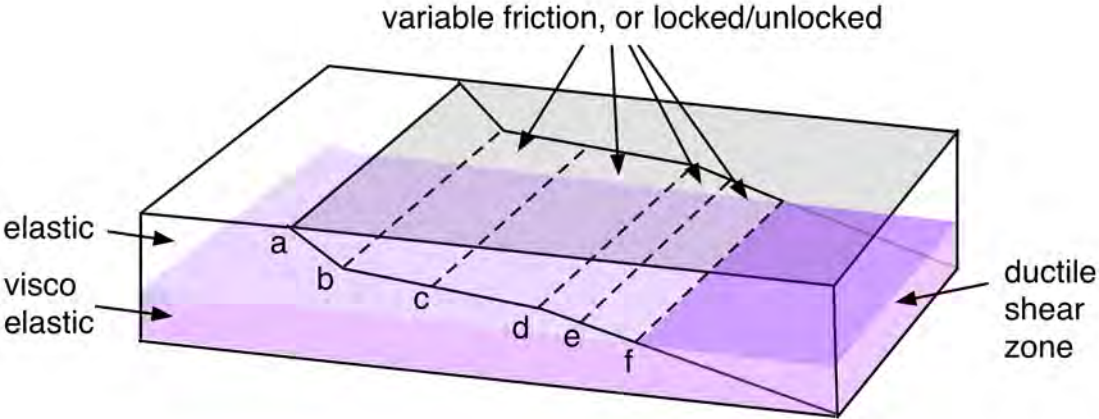
Figure M4. Model setup showing major mechanical domains, fault surface geometry, and patches for slip condition testing. The actual amount of afterslip on a patch of finite friction or free slip is calculated from the time dependent stress, and there is no requirement that patches move as coherent units, rather, these patches are only used to define the fault plane boundary conditions.

Table M3. Adapted arc-normal geometry of Main Himalayan thrust from Elliott et al., (2015)

	Y, arc-normal, km	Z, depth msl, km	Tectonic feature	Condition on segment below node
a	-80	0	MFT surface	Afterslip varies across simulations
b	-57.01	-8	Base MFT 19° ramp	Afterslip varies across simulations
c	-24.433	-12	Start 7° flat	Coseismic+ variable afterslip
d	22.99	-17.823	End 7° flat	Coseismic+ variable afterslip
e	37.214	-23	Base 20° ramp	Afterslip varies across simulations
f	53.503	-25	On 9° ramp	Afterslip varies across simulations
	all	-25	Brittle-ductile transition	10^{18}->10^{22} Pa s

Lower case letters in the first column refer to the transition boundaries in Figures S5, S6 and S7.
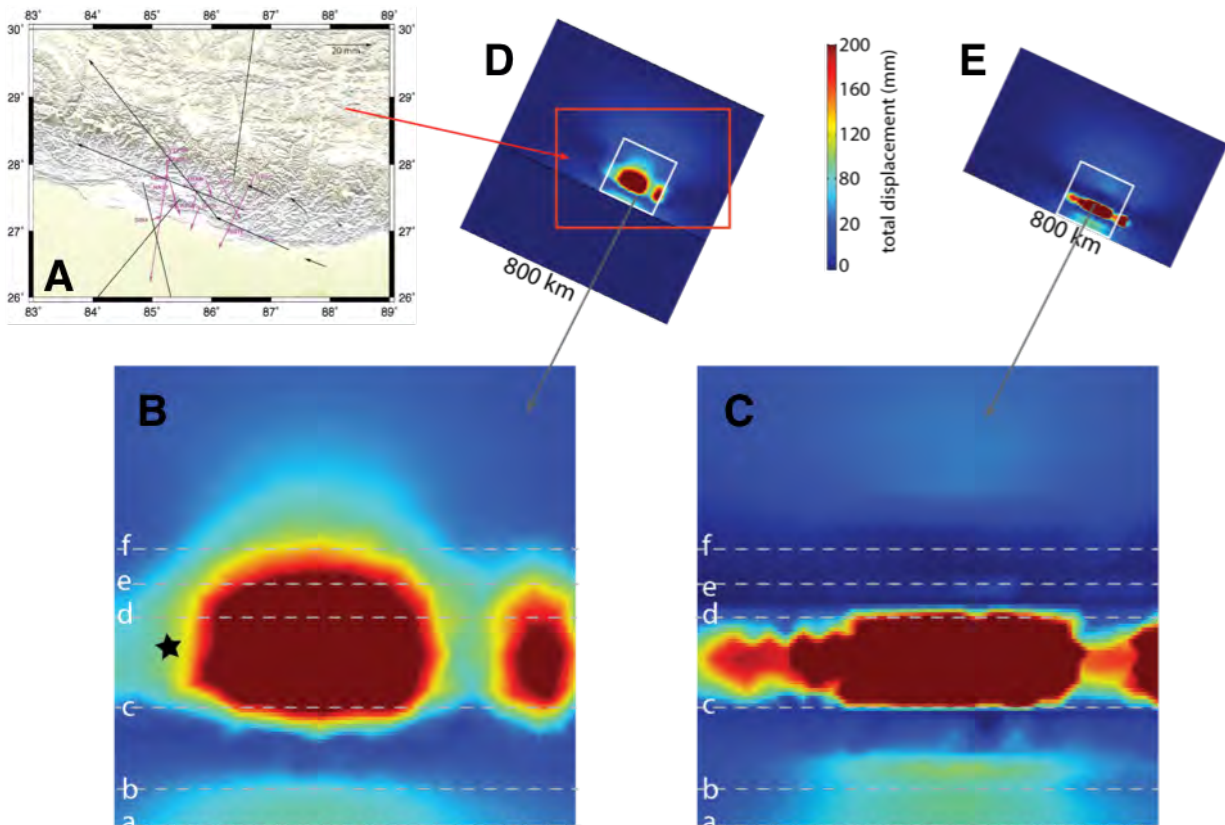
Figure M5. (a) Observed surface displacements 6-months after the main rupture (purple) and modeled displacements (black) for the same interval for simulations where the entire fault surface has free afterslip. (b) Total surface displacement magnitude for the same model over the entire ±400 km x ±400 km model domain. (c) Total afterslip magnitude on the fault surface and brittle ductile transition.(d) enlarged view of b, (e) enlarged view of c. The dashed white lines indicate segment boundaries on the MHT as shown schematically in Figure S4 and as listed in Table S3. Small lower case letters a-f on the figures correspond to the boundaries. Star corresponds to the mainshock.

9
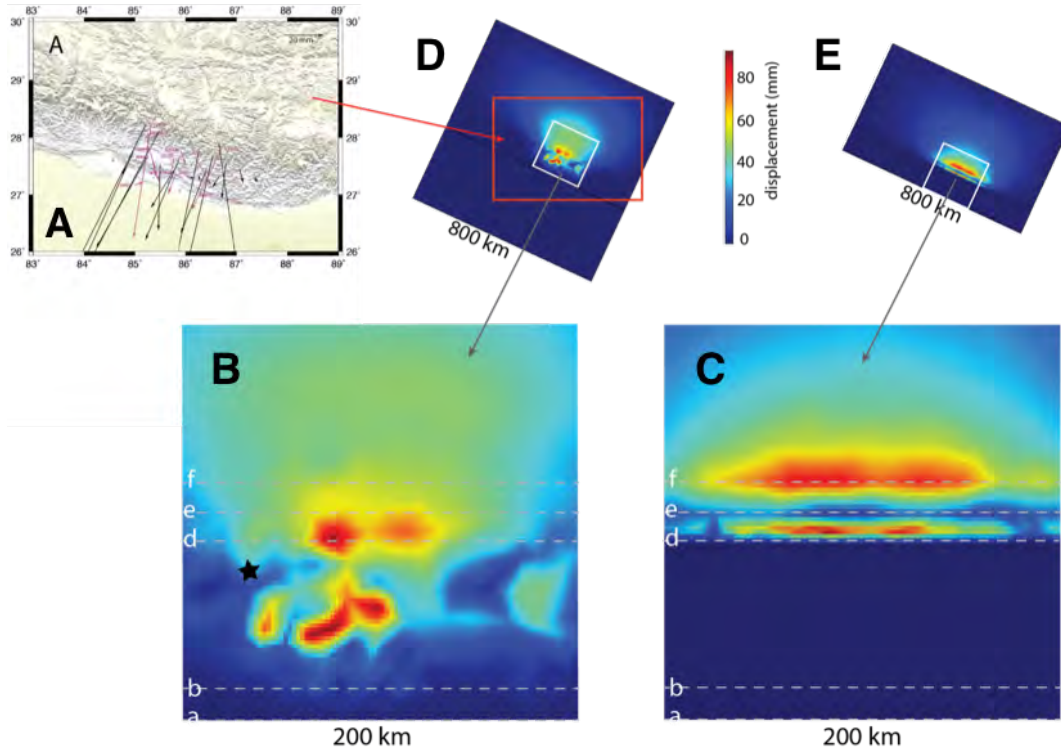
Figure M6. As in Figure M5 but with afterslip allowed on all fault plane segments below the coseismic rupture area.
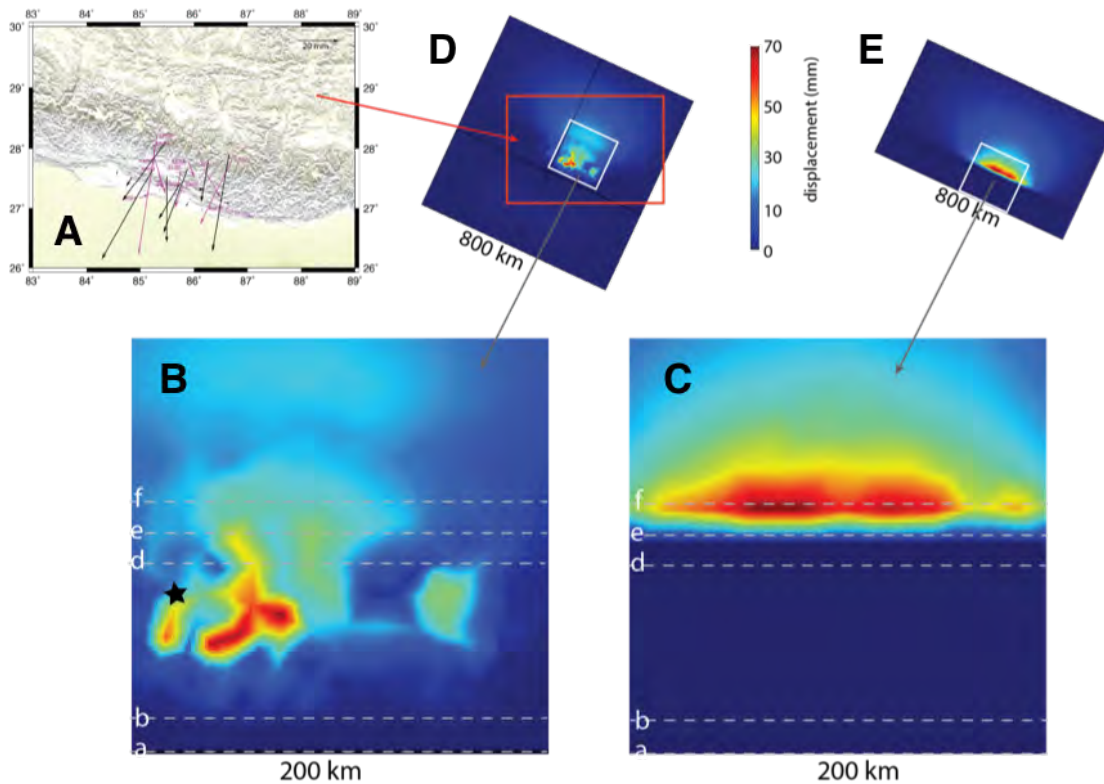
Figure M7. As in figure M5 for the preferred model. We note a difficulty is encountered in modeling the afterslip close to the down-dip edge of the rupture. Very large afterslip is predicted in the region contiguous with rupture, but we have few GPS data to constrain strain gradients here. Instead we examined end member models for both 3D (see section 4) and 4D models that approached the down-dip end of the rupture and concluded that the closed contours as shown in this figure obviously fill the region between coseismic slip and afterslip. We chose to leave these contours open in Figure 1 of the main text in deference to this physical reality and because of the absence of observational constraints.

3. (A) Similar magnitude and location of the 1833 and 2015 Nepal earthquakes

The 1833 earthquake is known only from its reported felt intensites[10,15]. Attempts to identify the epicenter and its magnitude (Figure M8) have used contouring methods and their contained areas[10,26], kriging methods[2] and a method developed by Bakun and Wentworth (1999) with its assumed ability to provide an objective repeatable epicentral location and magnitude[1,30]. The listed locations and magnitudes in Szeliga et al., (2012) are stated by these authors to be unreliable since they demonstrate an inherent weakness in the Bakun & Wentworth method where data are spatially sparse or biased to one side of the rupture, as is the case for the 1833 earthquake. Notwithstanding the different methods adopted, most of the published epicentral locations lie close to the rupture zone of the recent earthquake and its aftershocks. With the exception of the GEM-favored analysis (December 2015) whose authors use few data intensity data from Nepal or India, the magnitudes lie in the range 7.5<Mw<7.9.
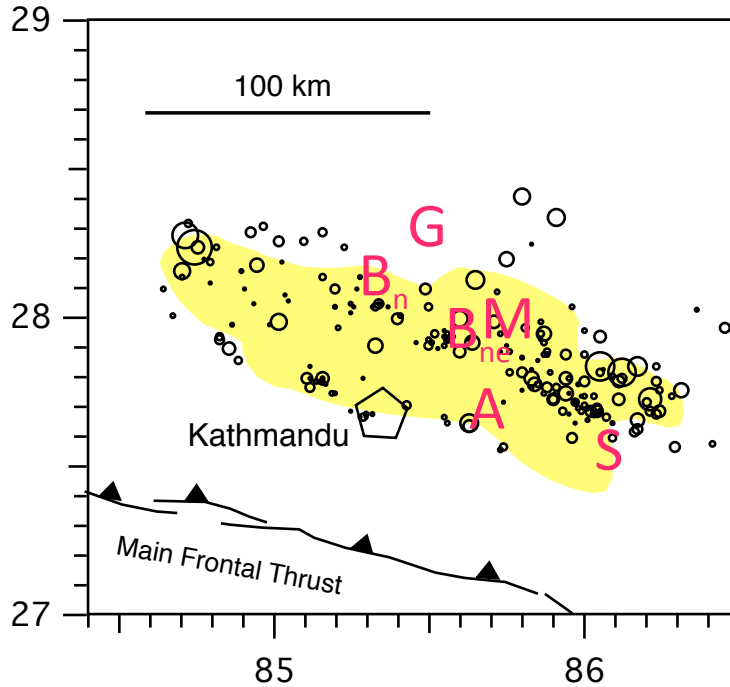
11

Figure M8. Locations for the 1833 earthquake derived from macroseismic observations: Bn and Bne, Mw7.7±0.2 Bilham (1995); A = Mw7.6, Ambraseys and Douglas (2004); S= Mw7.5, Szeliga et al., 2010, G=Mw8.0; GEM historical archive (Albini et al., 2013); M=Mugnier et al., 2014. The yellow area is the inferred rupture zone of the 2015 earthquake. The Kathmandu valley is shown by a pentagon.

There is thus no doubt that the two earthquakes were similar both in magnitude and location. In this supplement we examine the decay of EMS intensity with radial distance for the 1833 and 2015 earthquakes using a polar plot with a logarithmic radial distance ordinate. The plot emphasizes differences in the mezzo-central region and de-emphasizes observations far from the rupture, which due to their great distance do not influence interpretations of the finite area and location of rupture. The radial plot has utility in highlighting differences between earthquakes with similar magnitudes and approximately similar locations.

We first itemize seventy one intensity data obtained by the authors during the course of the GPS measurements above the rupture zone (Table M3). Photographs of these assessment locations are available at http://cires1.colorado.edu/~bilham/Gorkha_Intensities/Intensities_2105.htm. (last accessed 21 Dec 2015). The map (Supplementary Figure M9) shows the locations of these 2015 EMS assessments as a colored circle, with the location of 1833 observations listed by Martin et al., (2015) as a black number. In figure M10 the 1833 and 2015 intensities are compared.
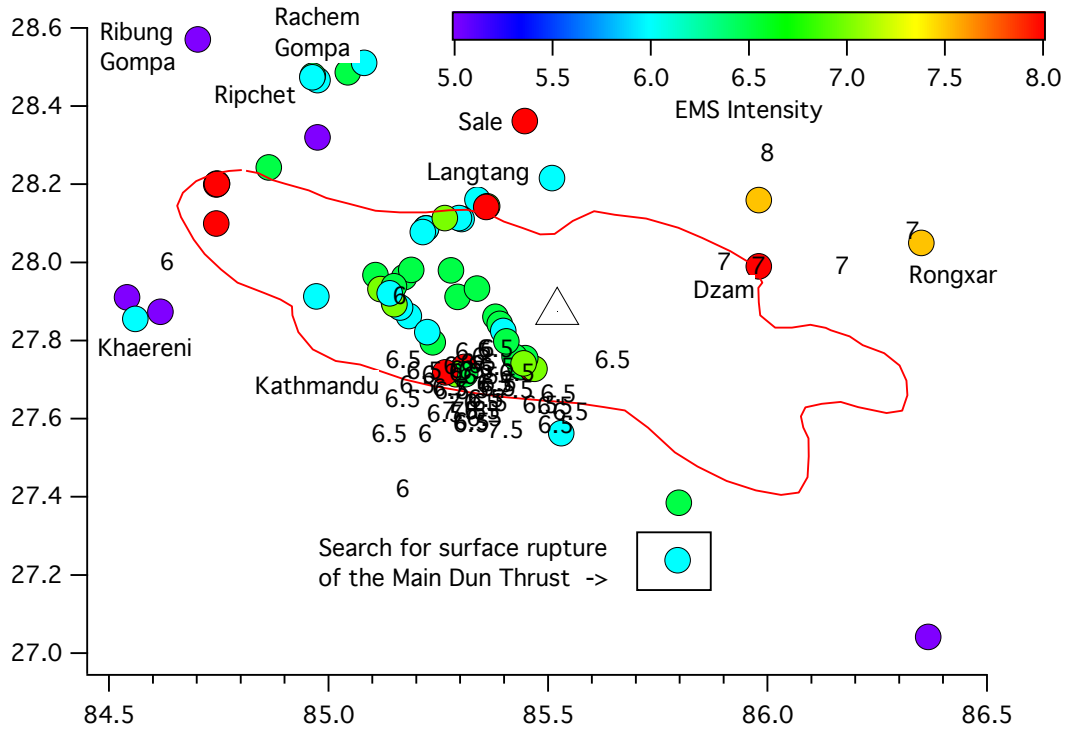
Figure M9. Mezzocentral intensity observations for the 1833 (black numbers) and 2015 earthquakes (colored circles), and the geographic center (triangle) used in comparison figure M10. The inset square indicates the location of the search for surface rupture (figures M10-M15).

Table M4. Observations of EMS Intensity in May 2015 used in comparisons between the 2015 and 1833 earthquake. Sites in Tibet were not visited, and were assessed from Chinese news reports.

Long	Lat	EMS	LOCATION	SUMMARY
84.746	28.202	7	Barpak	major damage to masonry, some damage to RC.
84.744	28.2	8	Barpak foundation column failure	RC house intact, 4 foundation columns splintered & bent.
84.744	28.1	8	Barpak ridge	total masonry collapse, damaged pillars in base of RC
84.746	28.201	8	Barpak ridge fissures	Ridge fissures ENE for 4
85.149	27.898	6.5	Batar Bazar	masonry minor collapse, RC unscathed
85.172	27.962	6.5	Bhaise	masonry major collapse
85.339	28.161	6	Chilime Trishuli bridge	masonry minor collapse, RC unscathed
85.044	28.487	6.5	Chokang Paro	masonry collapse- some still standing
85.183	27.863	6	Deorali	rc unscathed; masonry minor damage
85.303	28.111	6	Dunche New town	masonry minor collapse, rc unscathed
85.297	28.114	6	Dunche Old town	masonry minor collapse, rc unscathed
85.98	27.99	8	Dzam	News media photos of damage
86.597	26.991	5	Gaighat	undamaged masonry on ridge
85.107	27.968	6.5	Ghabran	masonry total collapse; minor damage to RC
85.163	27.885	6	Ghodghad	masonry minor collapse, rc unscathed
85.118	27.932	7	Goddhunga	masonry collapse; minor damage to RC
85.2222	28.0875	6.5	Gogne	major masonry collapse, rc unscathed.
85.222	28.087	6	Gogne	Trisuli slump on E. Facing mountainside.
85.29	28.86	7.5	Gyrong	Many stone rubble houses damaged
85.265	28.114	7	Haku	masonry total collapse; minor damage to RC
85.437	27.732	6.5	Indrayani	soft lower story RC collapse
85.303	27.725	7	Jagriti	soft lower story RC collapse
85.188	27.981	6.5	Kalikasthan	masonry total collapse; minor damage to RC
85.149	27.939	6.5	Khadakathock	masonry major collapse

13

85.237	27.796	6.5	Khaiekhel	masonry minor collapse
84.541	27.911	5	Khaireni	minor damage to weak masonry, RC unscathed
85.294	27.912	6.5	Kharentar	total masonry collpase, RC unscathed
84.864	28.243	6.5	Khorla	masonry wall collapse and roof loss
85.38	27.861	6.5	Kukre	minor masonry collapse RC unscathed
84.617	27.874	5	Kurintar on Prthivi River	weak fieldstone masonry collapse, RC unscathed
86.366	27.042	5	Ladbahir	no evident damage to village walls or structures
85.509	28.216	6	Langtang	masonry largely unscathed, lamps on shelf
85.39	27.843	6.5	Mahidan	masonry collapse minor rc damage
85.15	27.893	7	Majhitar	masonry total collapse; minor damage to RC
85.309	27.729	6	Mhaipi	undamaged RC frame
85.308	27.727	6	Mhyspi Ajima	no damage to RC
85.309	27.733	8	Mitranagar Sadak	Reputed former swamp. Severe damage to RC
84.56	27.856	6	Muglingmajor	masonry collapse , RC unscathed
85.98	28.16	7.5	Nyalam	News media photos of damage
85.53	27.563	6	Panauti	Brick masonry structures weakly damaged.
85.081	28.511	6	Rachem Gompa	dressed masonry OK, rubble walls collapsed
85.795	27.238	6	Raigun	liquefaction cracks 700 m long and 5 cm wide.
84.702	28.571	5	Ribung Gompa	No visible sign of damage to temple complex
84.975	28.32	5	Ridge at 4500 m	Numerous undisturbed precarious rocks on crest of ridge
84.975	28.467	6	Ripchet	flagstone masonry partly destroyed
84.964	28.478	6.5	Ripchet school west	interior stone wall collapsed-partial collpase external walls
84.963	28.474	6	Ripchet west 2 story house	2-story house, masonry separation, partial roof damage
86.35	28.05	7.5	Rongxar	News media photos of damage
85.447	28.362	8	Sa'le	Many stone rubble houses damaged
85.439	27.734	6.5	Sakharkande	major masonry collapse rc unscathed
85.462	27.729	8	Sankhu	masonry collapse, RCC minor damage. Worse on ridge.
85.469	27.728	7	Sankhu east	modest damage to masonry stupa
85.279	27.98	6.5	Sarangthal	masonry collapse, some survive
85.398	27.825	6	Shivarpur	partial masonry collapse
84.972	27.913	6	Simra	masonry collapse RC unscathed
85.225	27.822	6	Simwutar	rc unscathed; masonry collapse
85.798	27.385	6.5	Sindhulimadhi	weak stone masonry collapse Sindhulmadhi
85.448	27.755	6.5	Sundarija2	masonry collapse on bedrock edge of valley
85.424	27.759	6.5	Sundarijal	major masonry collapse rc unscathed
85.444	27.742	7	Suryamandali	Masonry damage to village along ridge
85.29	27.714	7	Swayanbhunath Temple	Ridge amplification masonry damage. RC little damaged
85.338	27.933	6.5	Thame	minor masonry collpase RC unscathed
85.311	27.714	6.5	Thamel	weak RC damage, masonry damage to large structures
85.361	28.144	7	Thulo Suabru	masonry total collapse; minor damage to RC, NW ridge
85.359	28.142	8	Thulo Suabru	masonry total collapse; major damage to RC, NW ridge
85.266	27.719	8	Thulu Bharyang	Significant damage to weak RC structures
86.63	28.57	6.5	Tingri	News media photos of damage
85.139	27.921	6	Trisuli	rc unscathed
85.2149	28.0781	6	Trisuli Landslide	No apparent shaking damage. Much landslide damage
85.405	27.798	6.5	Ukhreni	major masonry collapse rc unscathed
88.83	28.37	6.5	Xigatze	News media photos of damage

In each of the radial plots M10a and M10b we plot slant-distance data from geographic center of the 2015 rupture at 85.5°E, 27.9°N assuming a depth of 15 km (triangle in Figure M9). Figure M10a shows EMS data for 1833 and 2015 (Martin et al., 2015) supplemented by EMS observations from above the 2015 rupture listed in Table M4.
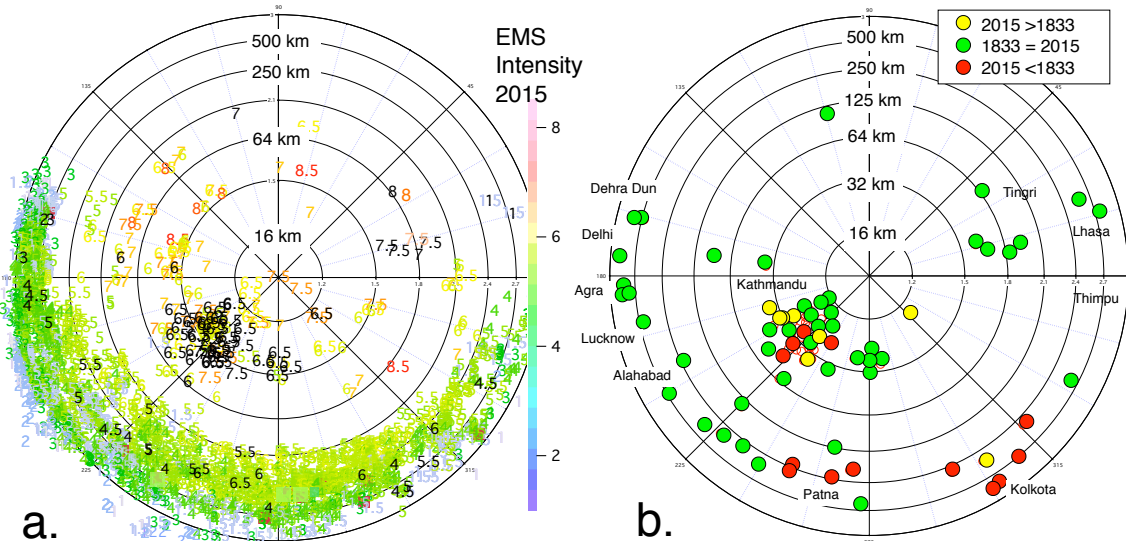
14

Figure M10. (a) polar plot of 1833 EMS numbered intensities black, 2015 intensities (Martin et al., 2015) numbered and colored with distances from the geographic center of the 2015 rupture (85.5°E, 27.9°N Figure S9). (b) differences of EMS shaking intensities for the 2015 and 1833 earthquakes for locations where shaking was observed in both earthquakes. Agreement (green indicates within 1 intensity unit, red or yellow indicates more than 1 intensity unit greater or smaller in 2015) prevails for most locations, and the numbers of excess and deficient intensities for 2015 -1833 are approximately equal.

The difference plot (Figure M10b) suggests that the two earthquakes were similar in magnitude and location. Were the 1833 earthquake 0.2 magnitude units larger or smaller than the 2015 earthquake, for example, the difference plot would have fewer green circles indicating differences less than 1 intensity unit. Were the earthquake significantly to the east or west it would have skewed the uniform coloring.

The cluster of high and low points in the Kathmandu valley in the SW quadrant of the rupture is presumably attributable to variations in reporting and local magnification effects because no systematic radial decay is evident. The cluster of "high" points near the Ganges (Patna) and in near Kolkota can be attributed to inflated intensities influenced by amplification effects insufficiently recognized in the 1883 reports.   For the purposes of this article we accept that the 2015 earthquake was very probably a close repeat of the 1833 earthquake and its aftershocks.

4.   Search for surface rupture near the Main Dun Fault 4 May 2015

No slip occurred on the Main Frontal Thrust (MFT) in April 2015, but initial interferograms showed a weak but persistent east-west discontinuity (Eric Fielding, personal communication, 1 May 2015) at approximately 85.73°E, 27.24°N northeast of the village of Kalpabrishykha and extending ≈25 km to the west near Raigaun. The west end of the discontinuity was visited to search for surface rupture. We identified a hairline crack and a liquefaction feature 27.2396N, 85.7258E but no thrust rupture. We evaluated EMS Intensity 6 from damage to structures in the 2 km x 2 km region near these features.
    The Insar discontinuity follows a forested ridge (Figure M11) but in the region inspected it crosses a north-flowing tributary to an east-to-west flowing anastomosing channel fronting hills to the north.

15

On landing a diligent search revealed no evidence for cracks in the river bed or the dry fields. However, in response to our enquiries about cracks in the ground subsequent to the earthquake, the villagers responded eagerly by showing us first a hairline fissure approximately 800 m north of the coordinate inferred from the interferogram and then a much larger fissure that had ejected water and silt during the earthquake approximately 1 km to the SW.
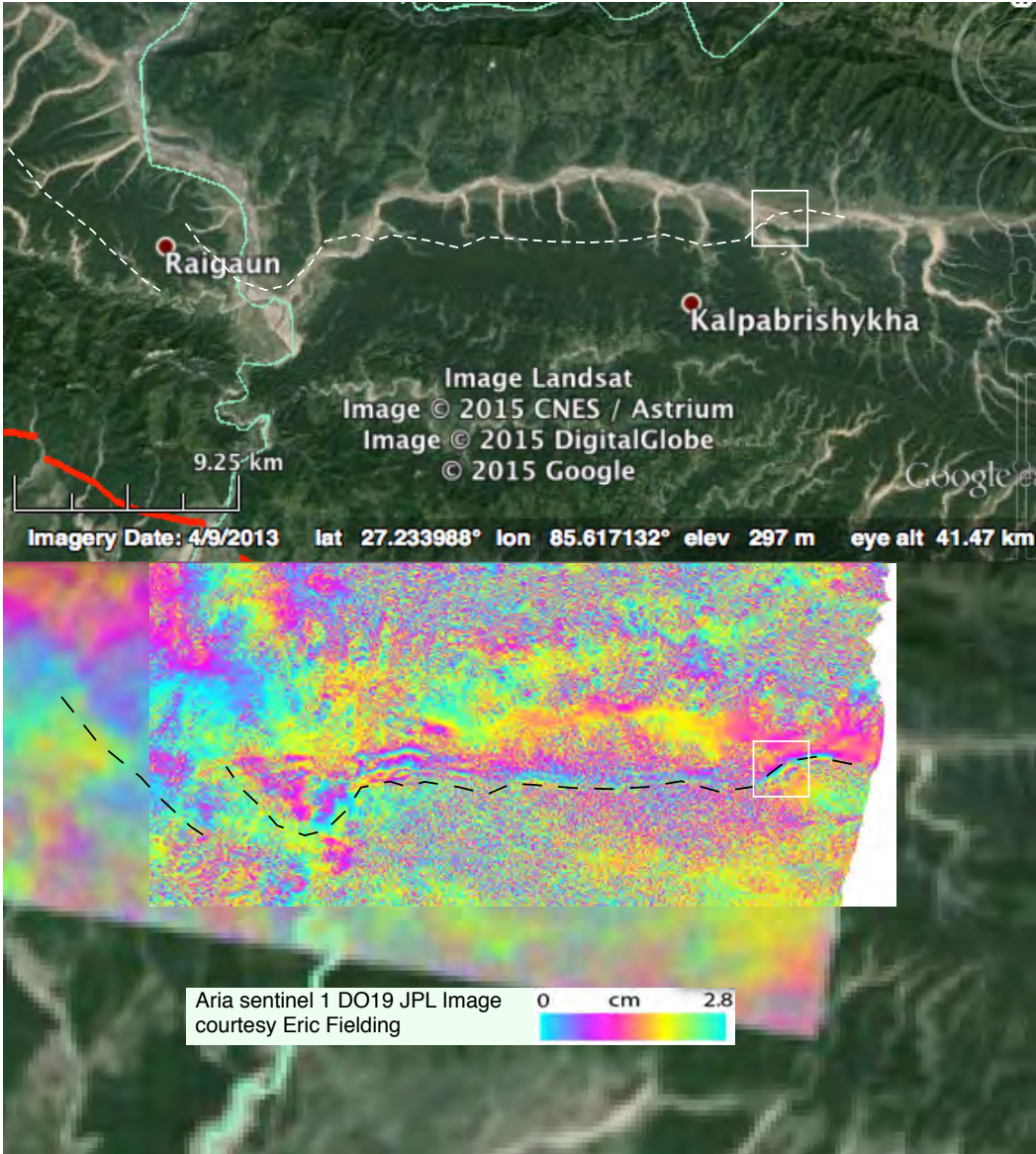
Figure M11. Image of 2-5cm dislocation in 1 May Aria Sentinel 1 scene (provided by Eric Fielding) for which we searched 4 May (white box shown in Figure M12).

Figure M12. Close up of inset region shown in Figure M11 consists of a 2-km-wide, anastomosing river channel with fields of agriculture near its edges leading to forested slopes of hummocky Siwalik hills. The approximate path of the Insar discontinuity is shown by a green dashed line. Black circle is landing spot for helicopter. Cracks identified by villagers shown as solid lines. Black squares approximate locations of high resolution images of river bed used unsuccessfully to locate fissures. Yellow dashed line region inspected on foot.

Figure M13. View north from the westernmost black box in Figure M12 at approximately 100 ft elevation.

The hairline fissure was east-west and about 10 m long and barely visible (ten days after the earthquake) where it had cut recent vehicle tracks in mud. It lay on eastern edge of the flood plain of the river close to the edge of a north-facing slope where it petered out amid a stiff clay covered hillside covered by bushes and trees (near the forested bluff on the right in Figure M13). No vertical or lateral offset was evident in this fissure.

Figure M14. Hairline fissure to north of initial search area viewed looking west.

The second fissure was also east west and about 650m long and was initially reported to exceed 10 cm in width and 2 m depth. It cut through a field of maize and passed near a cylindrical, concrete-lined water well. During the

17

earthquake (shortly after shaking commenced) both the well and the fissure expelled water and silt. After some tens of minutes this ceased and the fissure closed. The well was dry when we visited it. A thin layer of silt now covered the field downhill from the fissure, that at the time of our visit was nowhere wider than 2 cm. It is possible that the soils across the crack had been offset by 1-2 cm down to the north.

Figure M15 (left). 5 cm wide liquefaction crack with silt covering soil layer.

Fissures in the river bed had evidently resulted from shaking and liquefaction during the earthquake. An attempt to follow these fissures to east and west from the air was unsuccessful since their projection led to forested rough terrain (Figure M16), where it was impossible to land a helicopter or to view through the trees.

The intimate knowledge by the villagers of the fissures in their land (Figures M14,M15), suggested to us that had a rupture occurred in the region, the villagers would have noticed it. We concluded that the convergence or uplift feature visible in the image must have terminated in the subsurface.

The <5 km width of the local fringe perturbation north of the maximum gradient suggests that local southward slip was confined to the uppermost ≈2 km[3,20,21]. Slip may have been induced locally on one of two splays between the MFT and MBT[7]. Husson, et al., (2004) term these faults the Main Dun Thrust. Long term slip of the fault splay that slipped appears to be responsible for back-tilting the divide visible in Figure M11 northwards, confining the prominent east-west anastomosing channel to its northern edge against the mountain front visible in Figure M13. The back-tilting process is similar to that which confines the Jhelum to the northern edge of the Kashmir Valley[11].

Figure M16. View west from study area showing forest cover and hummocky terrain and an absence of landing sites.

18

Figure M17. Masonry structures (200 m south of the liquefaction fissure) showed no evidence for damage except of the loss of a few tiles near end gables (Intensity 5-6).

We flew 2 km west (Figure M16) searching for fissures and finding no evidence within the forest cover we flew east for 20 km. In the region within 4 km of the fissure search we inspected building damage and found that a few houses had lost their tiled roofs but most, like those near the fissure had no visible damage. Of the 50 dwellings we inspected, only one family had erected a tent suggesting that the roof damage and expectation of damage to walls from aftershocks was minimal. We assessed the region as EMS intensity 6 noting that liquefaction was confined to the river sediments, and all dwellings were on the Siwalik formation through which the rivers have eroded.

5. **Coseismic and post-seismic behavior of the MDT fault**

Elliot et. al, 2016, noted a maximum of 6 cm LOS displacement at the surface trace of the Main Dun Thrust (MDT) Sentinel A-1 data obtained on 17th April and 29th April 2015. We examine both the co-seismic and post-seismic contributions behaviour of the Main Dun Thrust (MDT) supposing it to represent a frictionless dislocation dipping 38° north intersecting the surface. We use a boundary element formulation[16] coded by Gomberg and Ellis (1994) to calculate slip on the MDT in response to coseismic slip[31]. This yields a maximum slip of 4.5 cm on the MDT (Figure M19), which is close to the observed surface slip. Since our formulation is friction free and ignores the Coulomb failure conditions which would tend to increase fault-normal stress, thereby reducing slip when exposed to the static strains from thrust faulting to the north of the MDT, we conclude that dynamic strains are responsible for reducing friction and causing amplified slip on the MDT.

19
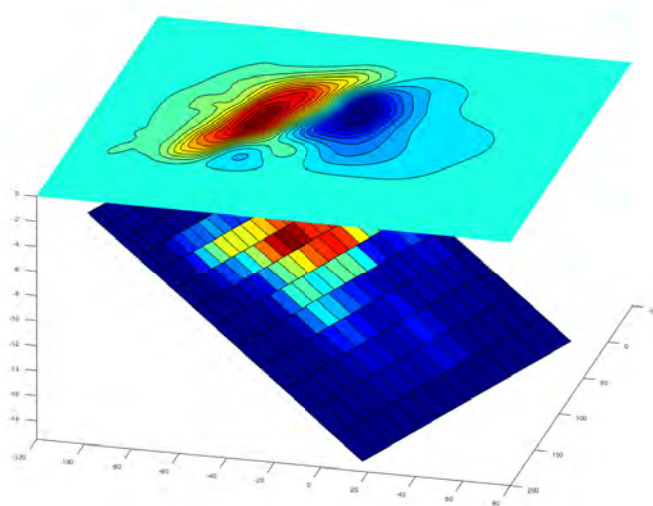
Figure M18. Input to the boundary element model used to estimate slip on the MDT. Calculated vertical displacements, plotted on the contour surface at z=0 along with the input slip geometry plotted on the dipping planar surface. Input slip geometry is from Wang and Fialko, 2015 using combined geodetic data from InSAR (ALOS-2) and GPS. Wang and Fialko examine both planar and listric solutions to accommodate the two-ramp flat geometry proposed by Avouac et al., 2015. We use this verify our model geometry. Axes scale is in km, fault plane scale is 0-10 m and surface displacement scale is from - 2 m to +2 m.

The co-seismic deformation observed in the model accounts for approximately 75% of the observed slip on the MDT, although the model favors a maximum displacement to the east, as opposed to the west as was observed. We suspect that the maximum displacement is sensitive to local geometries in the model. The co-seismic displacement on the plane of the MDT is shown in figure M19.
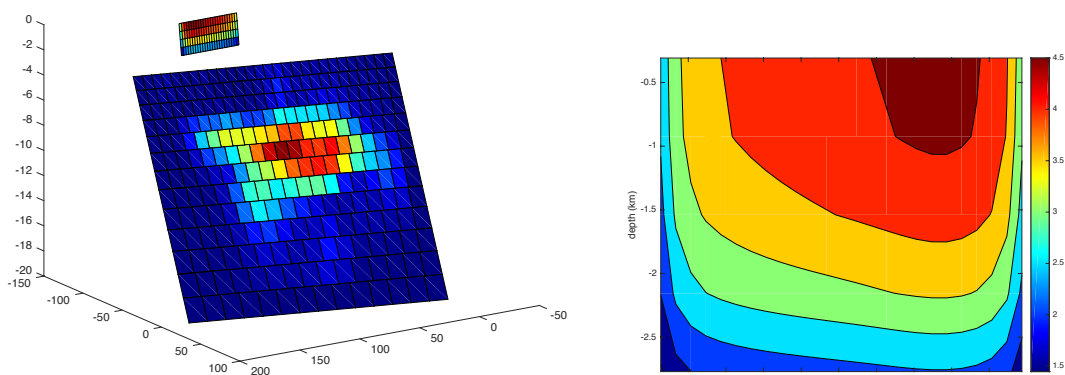
Figure M19. Modeled co-seismic down-dip slip on the MDT (in cm) using the computed coseismic slip on the MHT as input by Wang and Fialko as input. West is to the left, and the top of the model is the earth's free surface. Maximum slip on the MDT occurs at the surface. Axes scale is in km.

Having approximated the triggered slip on the MDT we proceed to use this triggered slip distribution, and the coseismic slip on the MHT terminating near Kathmandu[31], to constrain the maximum afterslip south of Kathmandu on the MHT. We allow the area between the locked top of the MHT and MDT to slip with zero friction, performing a χ^2 grid search for the best fit between our observed GPS data and the synthetic surface deformation from permitting various areas to slip south of Kathmandu. We find that the best fit to the surface data has highest slip near the southern edge of the Kathmandu rupture and tapers southward to zero slip roughly, 5 km south of the coseismic rupture. Figure M20 shows the best fitting afterslip (χ^2 = 2.9) on this unruptured surface. The mean slip on this interface is 2.5 cm. This ≈4 km wide southward tapering region of afterslip places a maximum bound of afterslip in this region south of Kathmandu.

20
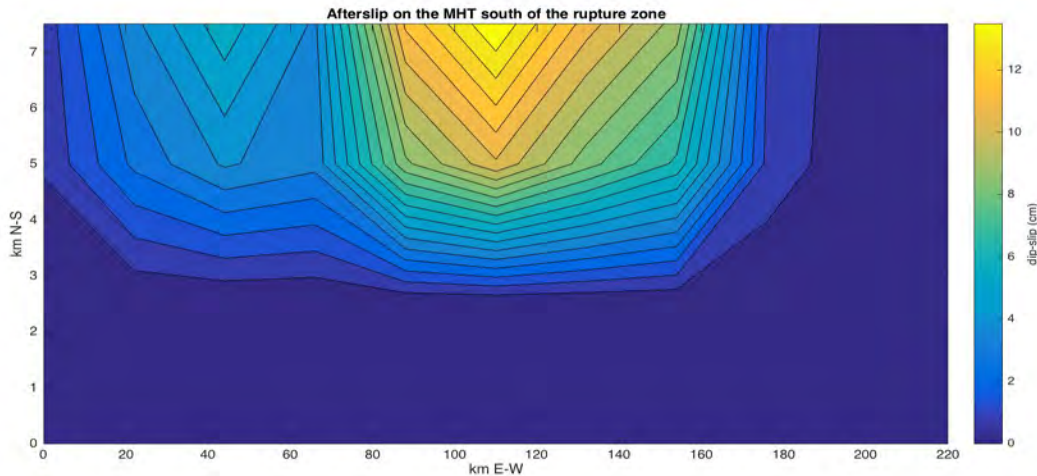
Figure M20. Modeled down-dip afterslip on the MHT south of the rupture zone (in cm).

References

1. Albini, P., R.M.W. Musson, A. Rovida, M. Locati, A.A. Gomez Capera, and D. Viganò, (2014). The Global Earthquake History, *Earthquake Spectra*, 30, 2, 607-624.
2. Ambraseys, N. and Douglas J.J., (2004), Magnitude calibration of north Indian earthquakes, *Geophys. Journal International*, 159, 1, 165-206
3. Angster, S., E. Fielding, S. Wesnousky, I. Pierce, D. Chamlagain, D. Gautam, B.N. Upreti, Y. Kumahara and T. Nakata, (2015), Field reconnaissance after the April 25 , 2015 M7.8 Gorkha earthquake. Seism Res Lett.
4. Argus, D.F., Gordon, R.G, and DeMets, C. Geologically current motion of 56 plates relative to the no-net rotation reference frame, (2011), *Geochemistry, Geophysics, Geosystems* , 12, Q11001.
5. Avouac, J.-P., L. Meng, S. Wei, T. Wang, and J.-P. Ampuero, (2015), Lower edge of locked Main Himalayan Thrust unzipped by the 2015 Gorkha earthquake, *Nature Geoscience*, **8**, 708–711.
6. Bakun and Wentworth, (1977), Estimating earthquake location and magnitude from seismic intensity data, *Bull. Seism. Soc. Amer*, 87, 1502-1521.
7. Bashyal., R. P.,(1998) Petroleum exploration in Nepal., *J. Nepal Geological Society*, 18, 19-24
8. Bendick, R., S. F. Khan, R. Bürgmann, F. Jouanne, P. Banerjee, M. A. Khan, and R. Bilham (2015), Postseismic relaxation in Kashmir and lateral variations in crustal architecture and materials. *Geophys. Res. Lett.*, 42, 4375–4383.
9. Bertiger, W., S. Desai, B. Haines, N. Harvey, A. Moore, S. Owen, and J. Weiss, (2010), Single receiver phase ambiguity resolution with GPS data, *J. Geodesy*, 84(5), 327-337.
10. Bilham, R., (1995). Location and magnitude of the 1833 Nepal earthquake and its relation to the rupture zones of contiguous great Himalayan earthquakes, *Curr. Sci.* 69, 101–127.
11. Bilham, R., & B. S. Bali, (2013) A Ninth Century Earthquake-Induced Landslide and Flood in the Kashmir Valley, and Earthquake Damage to Kashmir's Medieval Temples, *Bull. Earthquake Eng.,*
12. 12(1) 79-109
13. Bird, P., (2003), An updated digital model of plate boundaries, *Geochemisty, Geophysics, Geosystems*, 4, 1027.

14. Bos, M.S., Fernandes, R.M.S., Williams, S.D.P., and Bastos, L., (2013). Fast Error Analysis of Continuous GNSS Observations with Missing Data, *J. Geod.*, Vol 87(4), 351-360

15. Bos, M. S. and Scherneck, H. G., http://holt.oso.chalmers.se/loading/index.html

16. Campbell, A. (1833). Further particulars of the earthquake in Nepal, *Journal of the Asiatic Society of Bengal*, 2, Misc. VI, 636-639, London.

17. Crouch, S. L., Starfield, A. M., & Rizzo, F. J. (1983). Boundary element methods in solid mechanics, *Journal of Applied Mechanics*, 50, 704.

18. Gomberg, J., and Ellis, (1994), Topography and tectonics of the central New Madrid seismic zone: results of numberical experiments using a three-dimensional boundary element program, *J. Geophys. Res*, 99, 20299-20,310.

19. DeMets, C., R. G. Gordon, D. F. Argus, and S. Stein, (1990), Current plate motions, *Geophys. J. Int.*, 101, 425-478.

20. DeMets, C., R. G. Gordon, and D. F. Argus, (2010), Geologically current plate motions, *Geophys. J. Int.*, 181, 1-80.

21. Elliott J.R., R. Jolivet, P.J. Gonzalez, J-P Avouac, J. Hollingsworth, M. P. Searle, V. L Stevens, (2016), Geometry of the Main Himalayan Thrust, *Nature Geoscience*, 9, 174-180.

22. Fielding, Eric J., C. Liang, S. Samsomov, P. Agram, M-H Huang, S. Sangha (2015), Three dimensional surface deformation from the M7.8 Gorkha earthquake and M7.3 aftershock in Nepal measured by SAR interferometry and pixel offsets. (in press).

23. Huang, M., Bürgmann, R., and Freed, A., (2014), Probing the lithospheric rheology across the eastern margin of the Tibetan Plateau, *Earth Planet. Sci. Lett.* 396, 88-96.

24. Husson, L., J-L Mugnier, P. Leturmy and G. Vidal., (2004) Kinematics and sedimentray balance of the sub-Himalayan Zone, western Nepal , in K. R McClay ed., *Thrust mechanics and hydrocarbon systems: AAPG Memoi,r* 82, 115-130.

25. Johnson, K., R. Burgmann, and J. Freymueller, 2009, Coupled afterslip and viscoelastic flow following the 2002 Denali Fault, Alaska earthquake, *Geophys. J. Int.* 176, 670-682.

26. Martin, S.S., S.E. Hough, and C. Hung (2015). Ground motions from the 2015 M7.8 Gorkha, Nepal, earthquake constrained by a detailed assessment of macroseismic data, *Seism. Res. Lett.,*86, 1524-1532

27. Mugnier, J.-L., A. Gajurel, P. Huyghe, R. Jayangondaperumal, F. Jouanne, and B. Upreti (2013), Structural interpretation of the great earthquakes of the last millennium in the central Himalaya, *Earth Science Reviews*, 127, 30-47.

28. Nilsson, T., Böhm, J., Wijay, D. D.,Tresch, A.,Nafisi, V.,Schuh, H., Path Delays in the Neutral Atmosphere, in J. Böhm and H. Schuh (eds): *Atmospheric Effects in Space Geodesy*, Springer Verlag, ISBN 978-3-642-36931-5, pp. 73-136, 2013.

29. Okada, Y., (1985), Surface deformation due to shear and tensile faults in a half-space, *Bull. Seism. Soc. Amer.*,75, 1135-1154,

30. Savage, J. C. (1983), A dislocation model of strain accumulation and release at a subduction zone, *J. Geophys. Res.*, 88(B6), 4984–4996,

31. Szeliga, W., S.E. Hough, S. Martin, and R. Bilham (2010). Intensity, magnitude, location, and attenuation in India for felt earthquakes since 1762, *Bull. Seism. Soc. Amer.*, 100, 570-584

32. Wang, K., and Y. Fialko (2015), Slip model of the 2015 *Mw* 7.8 Gorkha (Nepal) earthquake from inversions of ALOS-2 and GPS data, *Geophys. Res. Lett.,* 42, 7452–7458,

33. Ward, S. N., Pacific-North America plate motions: New results from very long baseline interferometry, 95, 21965-21981, 1990.

34. Zumberge, J. F., M. B. Heflin, D. *, J. Geophys. Res.* C. Jefferson, M. M. Watkins, F. H. Webb, Precise point positioning for the efficient and robust analysis of GPS data from large networks, *J. Geophys. Res.*, 102 (B3), 5005-5017

Appendix: Detailed time series from 28 GPS sites used to evaluate afterslip.

1. A page is devoted to each site in alphabetical order. At the top of each page is the site name from the UNAVCO archive and a summary of the numerical characteristics of the data. These numbers are entered into Table S1 of the supplement, on page 1.
2. A map shows the site location relative to the mainshock rupture.
3. For sites with pre-seismic data we show east and west components with spectrally estimated fits to the seasonal signal consisting of two sine waves and two cosine waves. We also show the effect of removing these derived series from the north and east data.
4. For all sites we show the **raw North time series in green**, two other time series are shown: (a) in red we show data used in this study, and (b) in blue corrected for monsoon loading and interseismic convergence between India and Tibet as follows:
   a. the interseismic velocity field. This may be derived for a least squares fit to the preseismic data if these exist. If no preseismic data exist for the site, the interseismic velocity is derived from an elastic backslip model using a mean convergence rate of 19 mm/yr, and its distance from the northern transition from locked décollement to interseismic creep. An exponential fit to these data are shown as a red line.
   b. The surface deformation signal resulting from monsoon loading was calculated from GLDAS seasonal hydrology data. This was removed from (a) and a least squares exponential fit to these data used to derive the cumulative afterslip for six months following the earthquake. We find that these under-estimate, by approximately 10%, those signals calculated by spectral methods where comparison is possible but the difference in the calculated outcome is within error. For consistency we use the GLDAS correction for all sites in this study.
5. From four continuous GPS sites with good signal-to-noise ratio we determined a mean decay time-constant of 43±2 days (see footnote to Table 1), which we then applied to data from sites installed at various times after the earthquake. From the resulting amplitude term in the exponential fit we extrapolated the observed data from t=0, the time of the mainshock, to t=180, six months after the mainshock
6. For sites with no clear afterslip trend we assessed the maximum afterslip from the noise level in the data.
7. Afterslip displacements at four sites was not manifest as simple exponential decay. GHER exhibited initial accelerated afterslip which after 100 days approached background levels. CHLM and SYBC were significantly perturbed by the main aftershock east of Kathmandu:

AIRP start t=18, end t=90, A=5.7, D_{180}= 8.24 mm

Sparse data caused by solar panel problems.
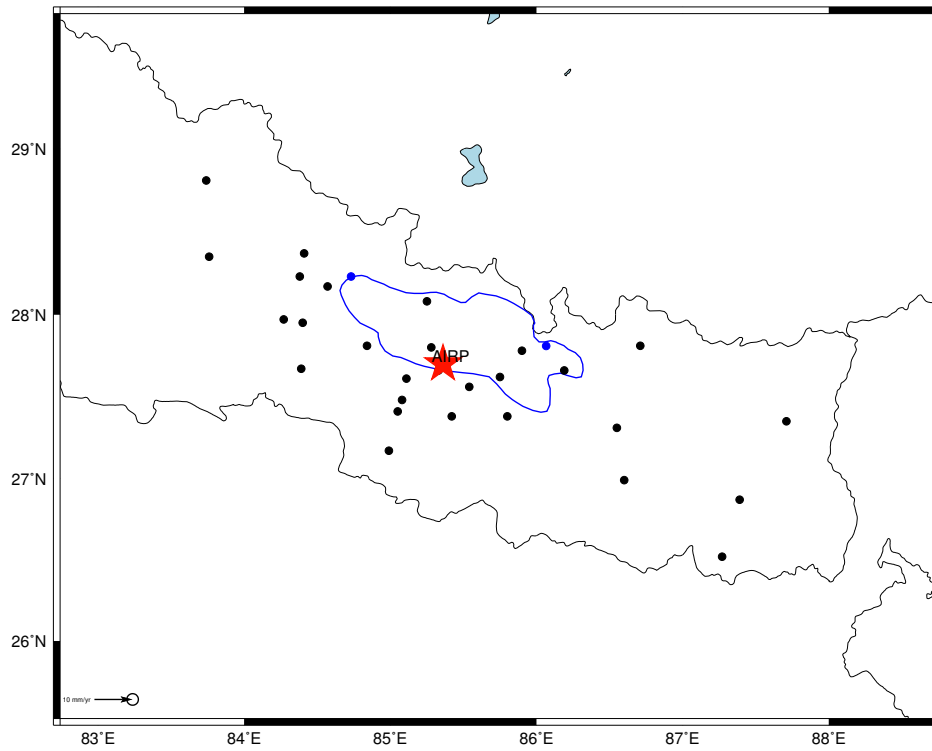
AIRP: A=5.7035 D(180)=-8.244

$f(t) = y0 + a \exp((16.5 - t) / 43)$
a = 5.7035
y0 = -3.039
R = 0.42513 (lin)
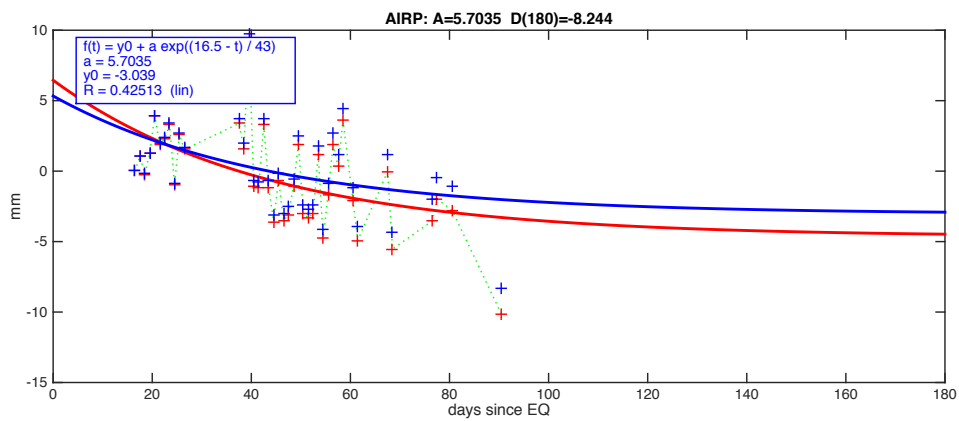
BESI start t=8, end t=110, A=1.9, D_{180}= 2.17 mm

No significant afterslip
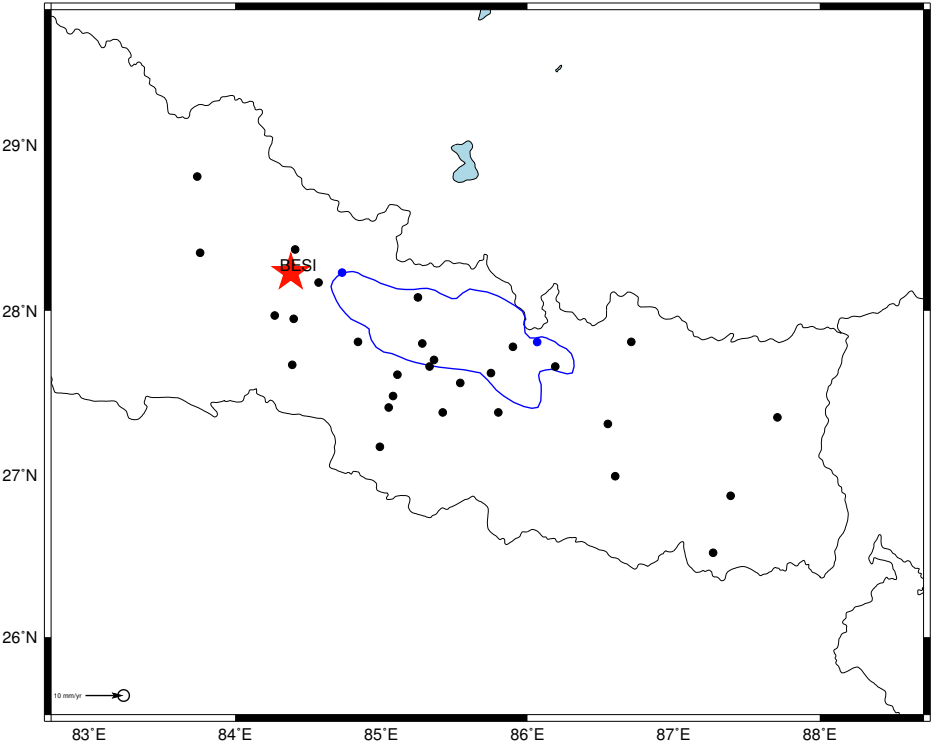
BESI: A=1.8911 D(180)=-2.1663

$f(t) = y0 + a\ exp((6.5 - t) / 43)$
$a = 1.8911$
$y0 = 1.0304$
$R = 0.18312\ (lin)$
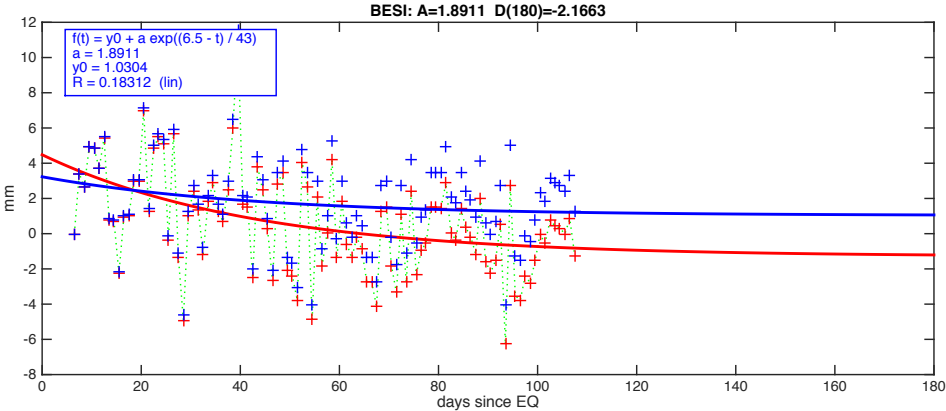
BNDP start t=7, end t=170, A=1.2, D_{180}= 1.4 mm

No significant afterslip
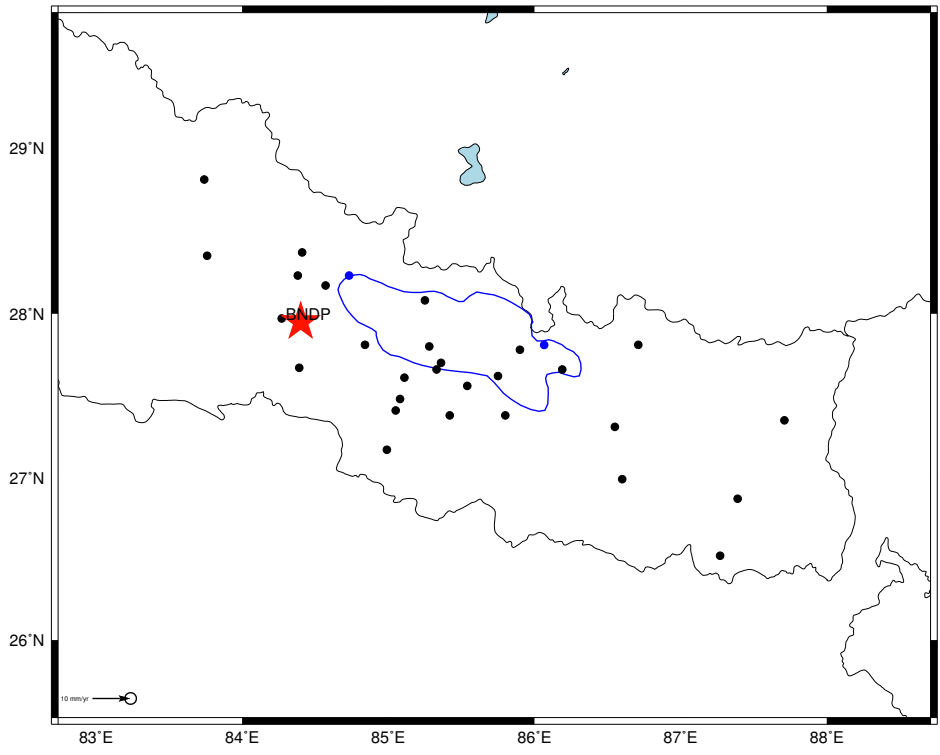
BNDP: A=-1.2361 D(180)=1.4493

$f(t) = y0 + a \exp((7.5 - t) / 43)$
$a = -1.2361$
$y0 = -3.6045$
$R = 0.13185$ (lin)

26
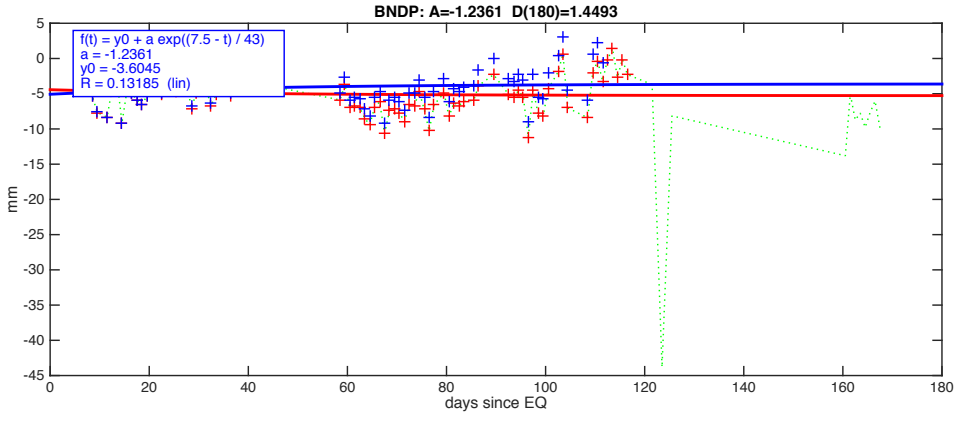
BRN2 start t=0, end t=170, A=0.6, D_{180}= 0.64 mm

No significant afterslip
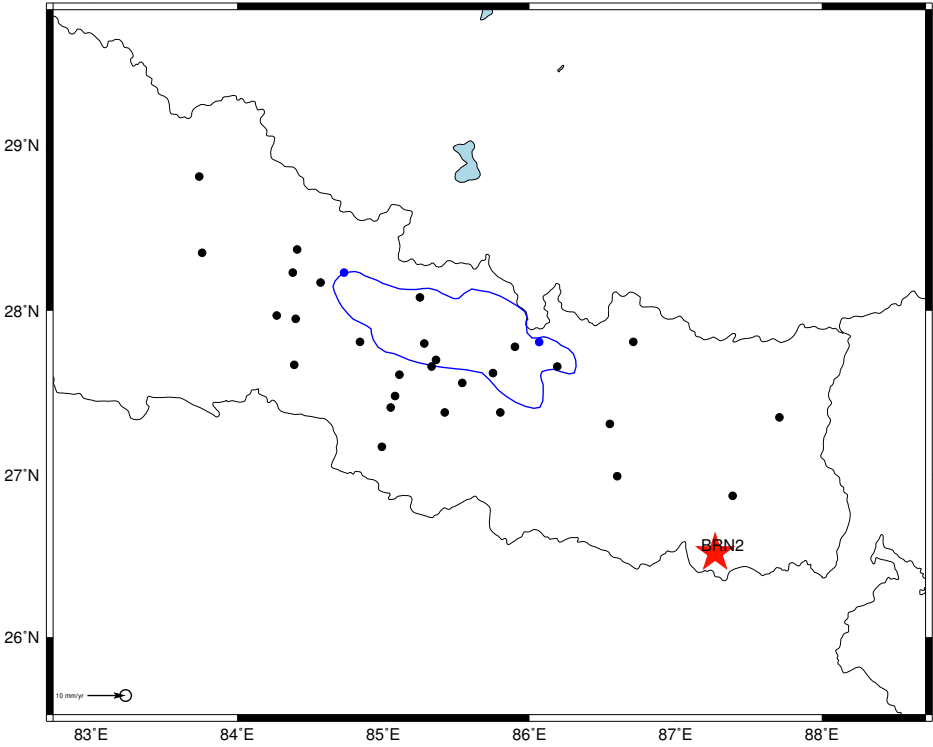
Image produced using p tdefnode.bash:Mencin/Vernant 2015 Version:1.32 Tue Dec 8 11:14:10 MST 2015

BRN2: A=0.62509 D(180)=-0.63744

f(t) = y0 + a exp((1.5 - t) / 43)
a = 0.62509
y0 = 0.95449
R = 0.065201 (lin)
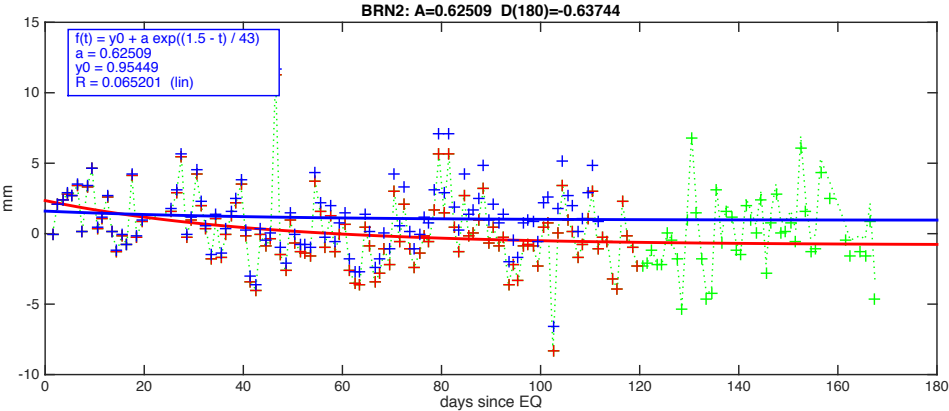
BTN1 start t=42, end t=170, A=4.6, D_{180} = 14.14 mm

No preseismic data. Time series starts 42 days after mainshock.
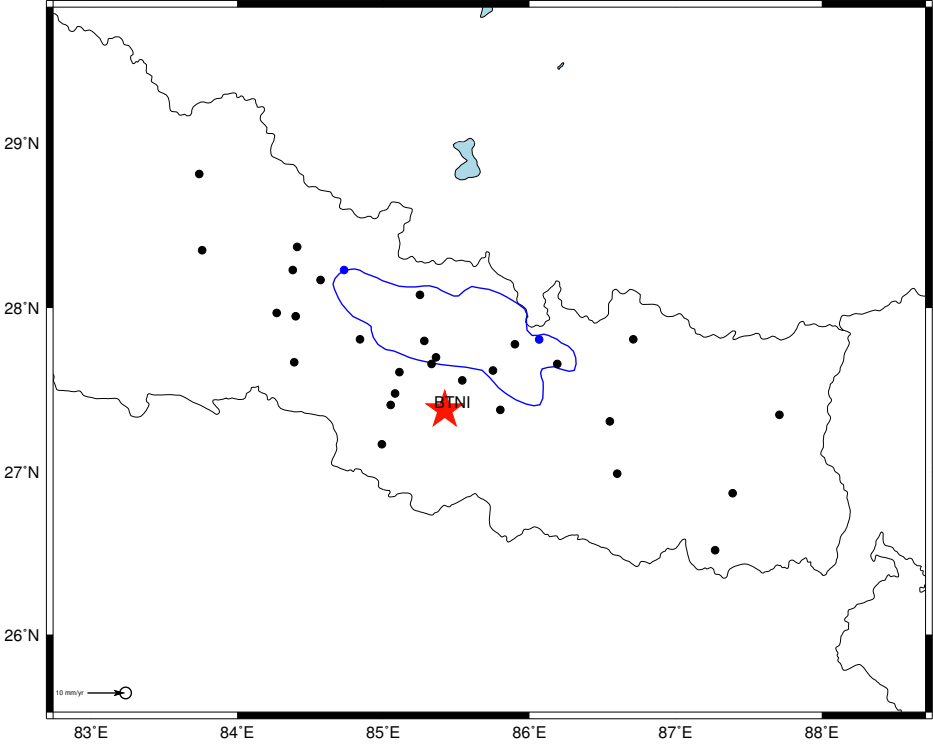
Image produced using p tdefnode.bash:Mencin/Vernant 2015 Version:1.32 Tue Dec 8 11:14:10 MST 2015

BTNI: A=4.6464 D(180)=-14.1353

f(t) = y0 + a exp((48.5 - t) / 43)
a = 4.6464
y0 = -2.7529
R = 0.45536 (lin)

28
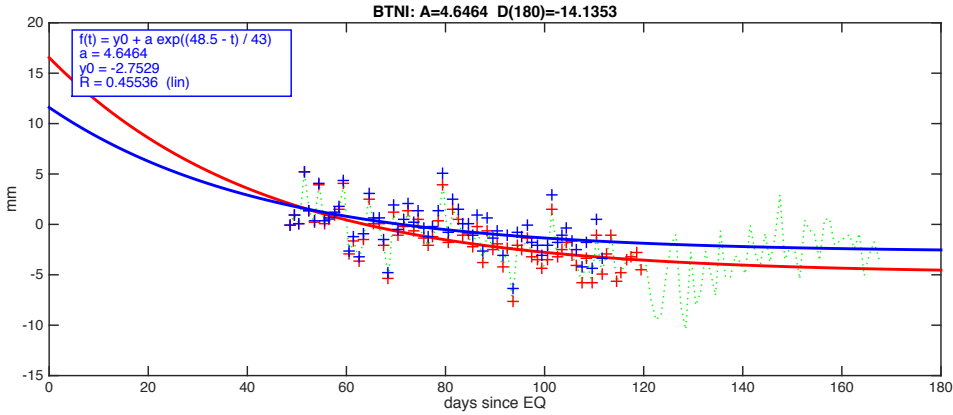
CHLM τ =63.4 days, A=55.4, D_{180}= 56.46 mm
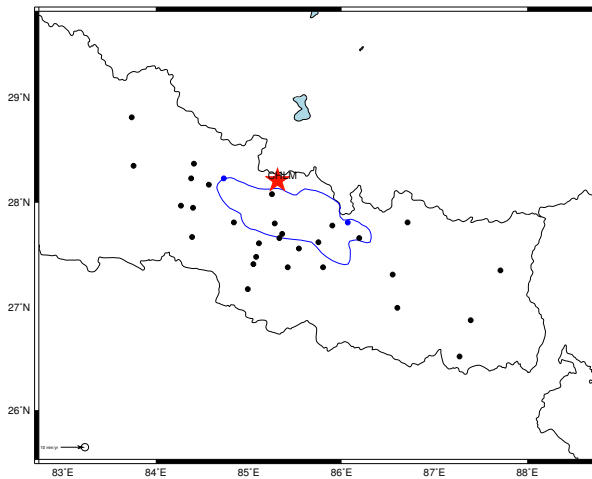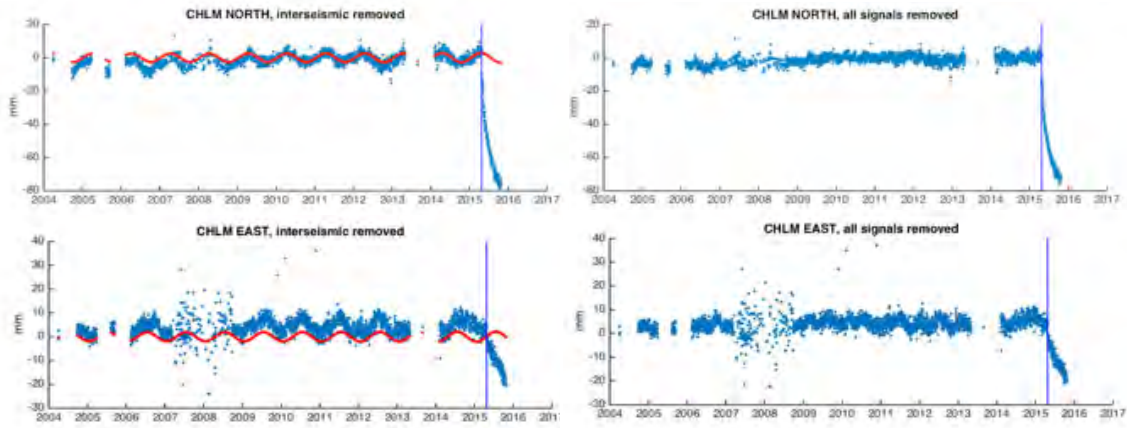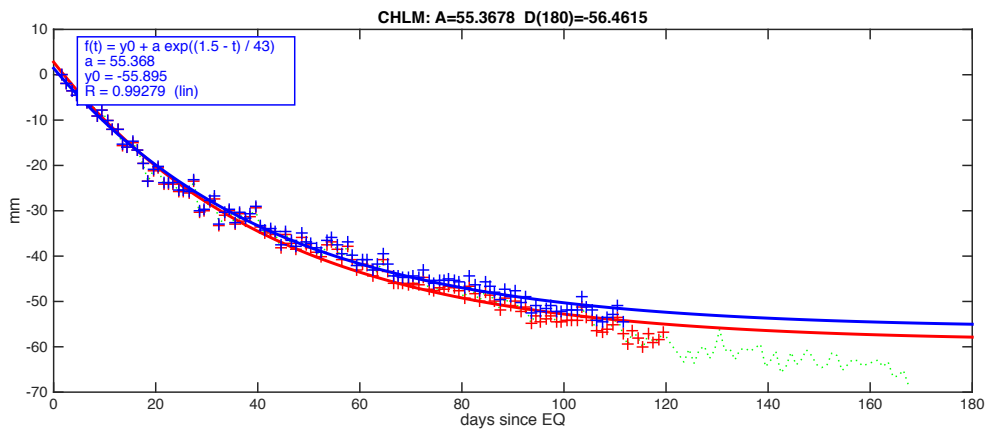
CTWN start t=5, end t=170, A=0.5, D_{180} = 0.58 mm
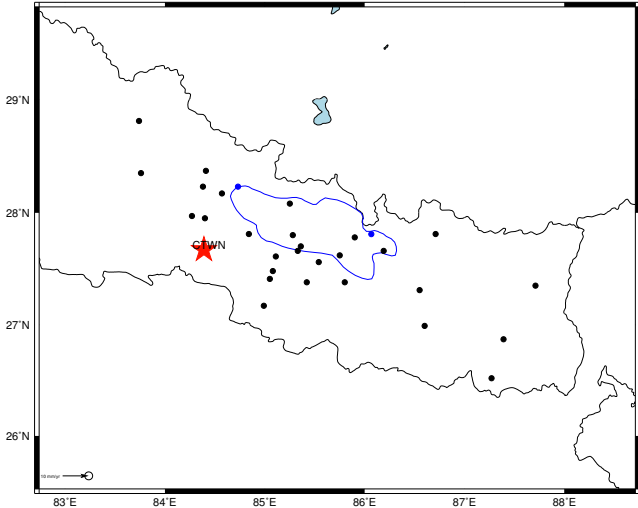
CTWN: A=0.5102 D(180)=-0.58444

f(t) = y0 + a exp((6.5 - t) / 43)
a = 0.5102
y0 = -5.9638
R = 0.057103 (lin)

days since EQ
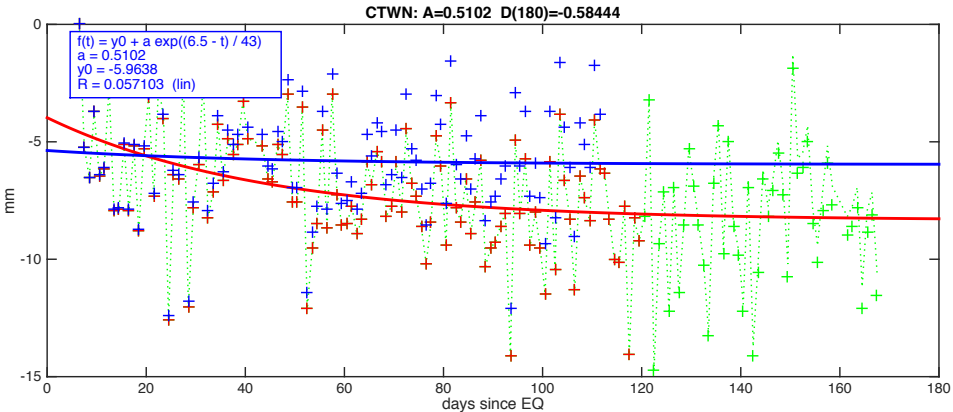
DAMN start t=12, end t=60, A=4 , D_{180}= 5.1 mm

No significant afterslip. Sparse data. Fit is artifact.
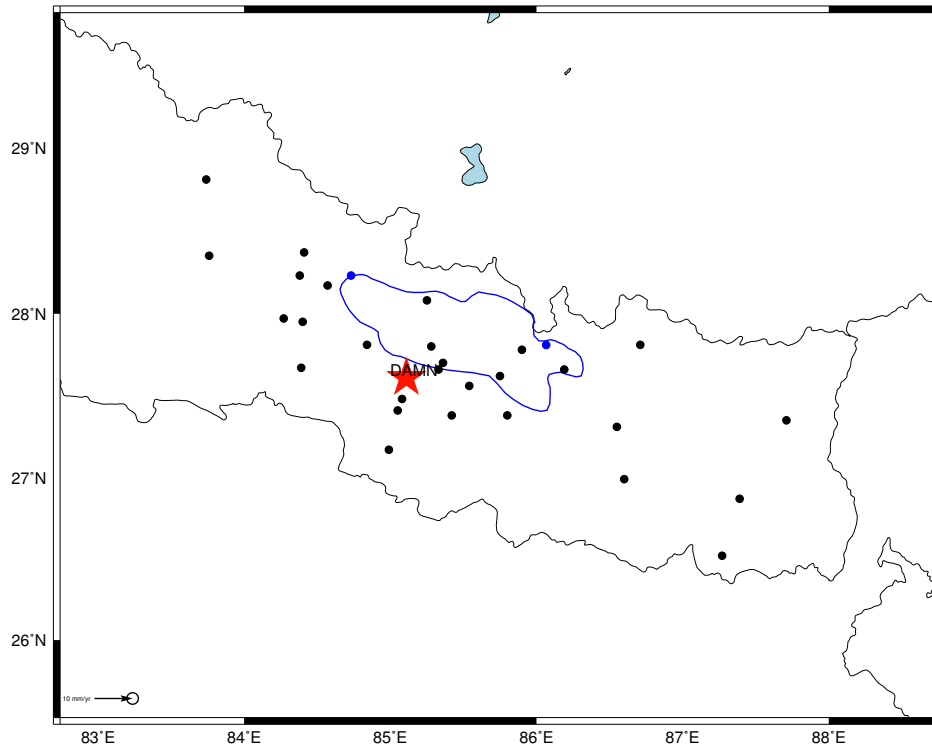
Image produced using p tdefnode.bash:Mencin/Vernant 2015 Version:1.32 Tue Dec 8 11:14:12 MST 2015

DAMN: A=-4.0204 D(180)=5.1732

f(t) = y0 + a exp((11.5 - t) / 43)
a = -4.0204
y0 = 1.6792
R = 0.32714 (lin)
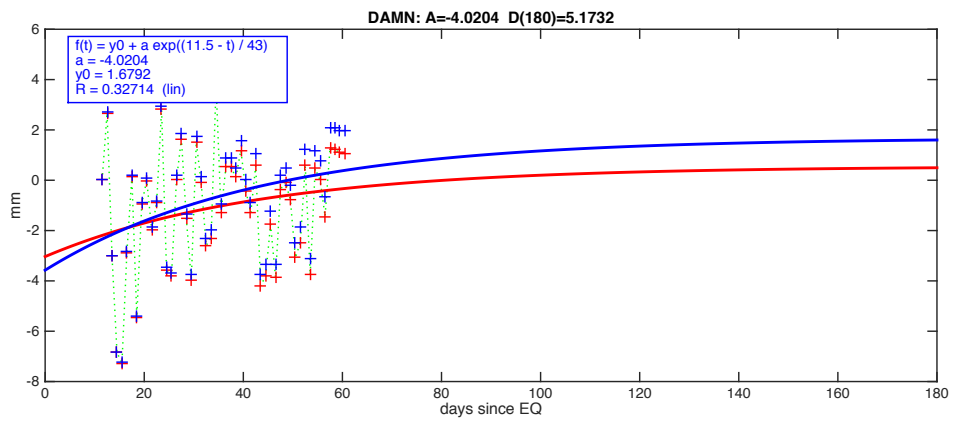
DMAU start t=0, end t=110, A=0.9, D_{180} = 0.96 mm

DMAU: A=0.94398 D(180)=-0.96263

f(t) = y0 + a exp((1.5 - t) / 43)
a = 0.94398
y0 = 2.2178
R = 0.082837 (lin)

days since EQ

DNC4 start t=52, end t=170 , A= 10.9, D_{180}= 40.07 mm
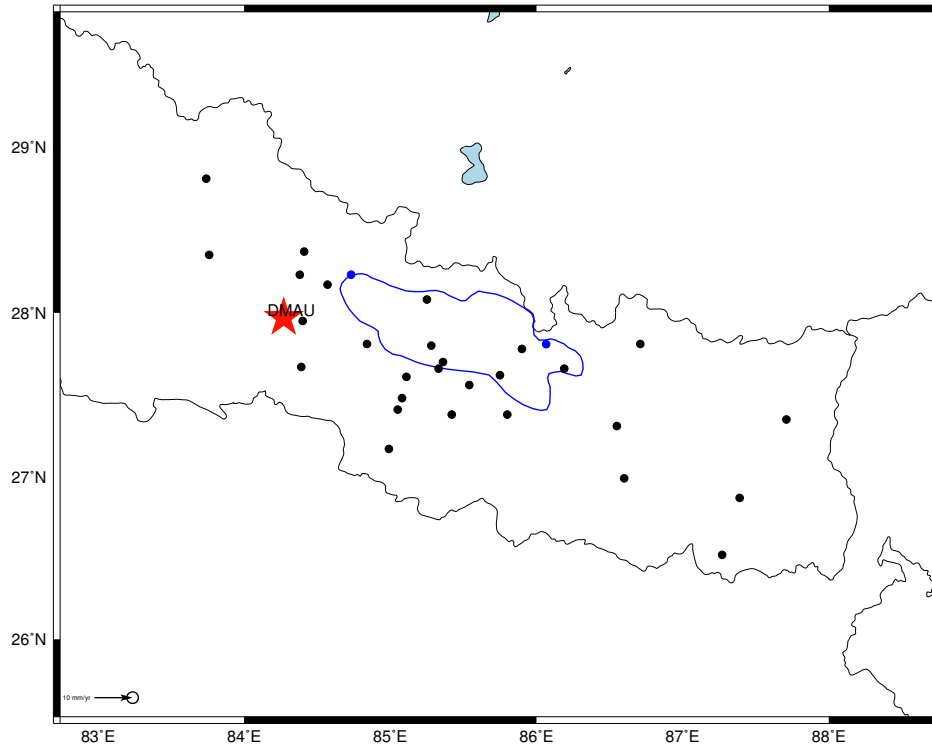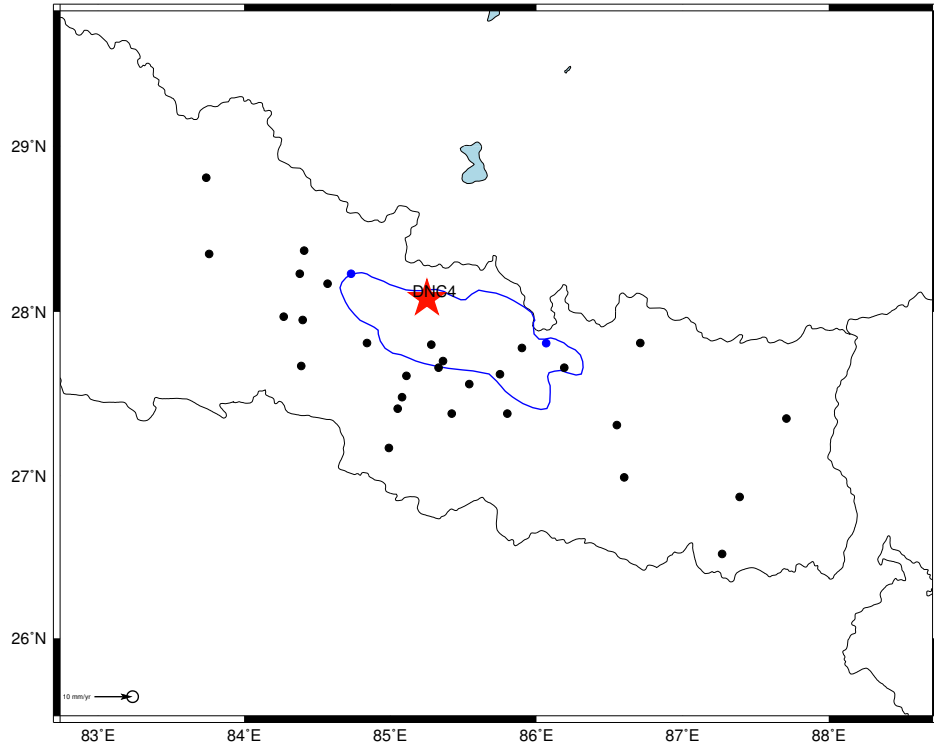
Image produced using p tdefnode.bash:Mencin/Vernant 2015 Version:1.32 Tue Dec 8 11:14:13 MST 2015

DNC4: A=10.9348 D(180)=-40.0681

f(t) = y0 + a exp((56.5 - t) / 43)
a = 10.935
y0 = -7.3432
R = 0.73846 (lin)

33
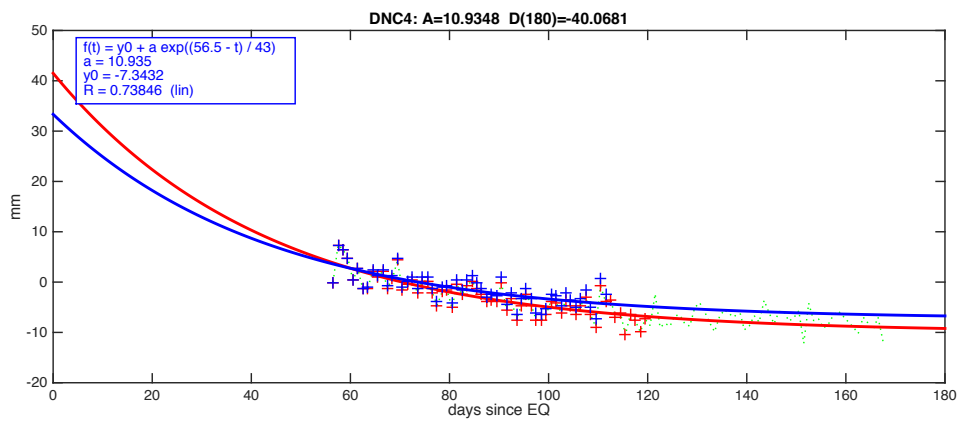
DNSG start t=0, end t=120, A=2.3, D_{180}= 2.33 mm
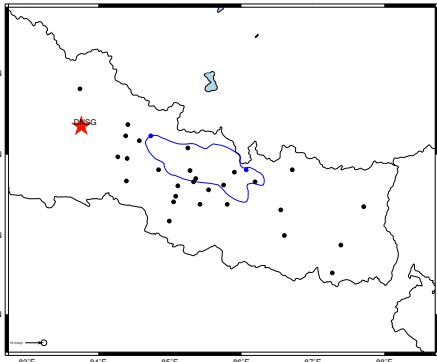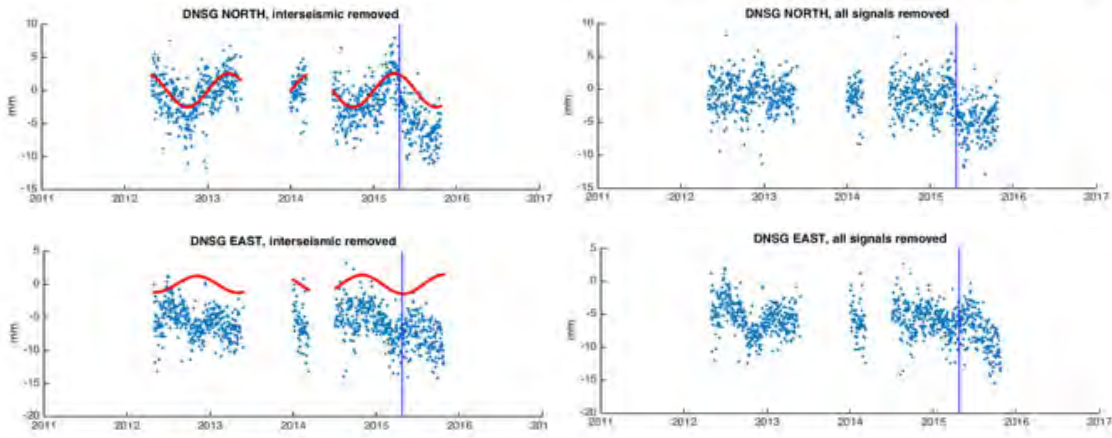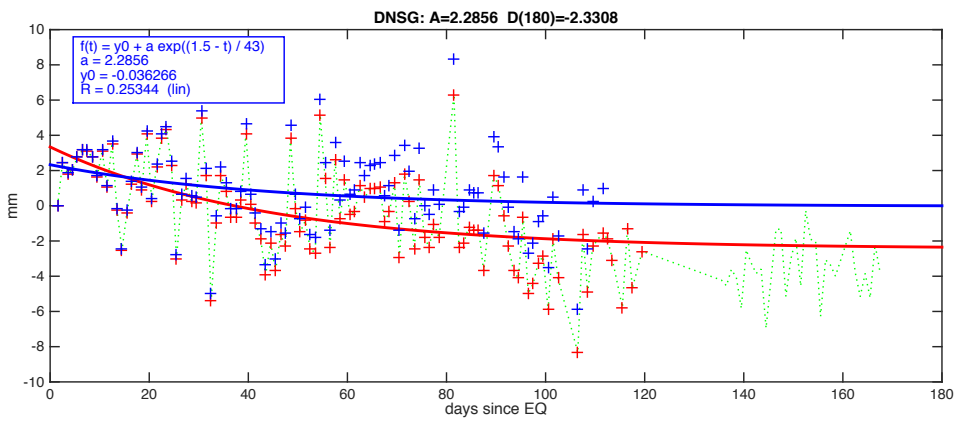
GHER start t=0, end t=95, A=7.7, D_{180}= 7.83 mm
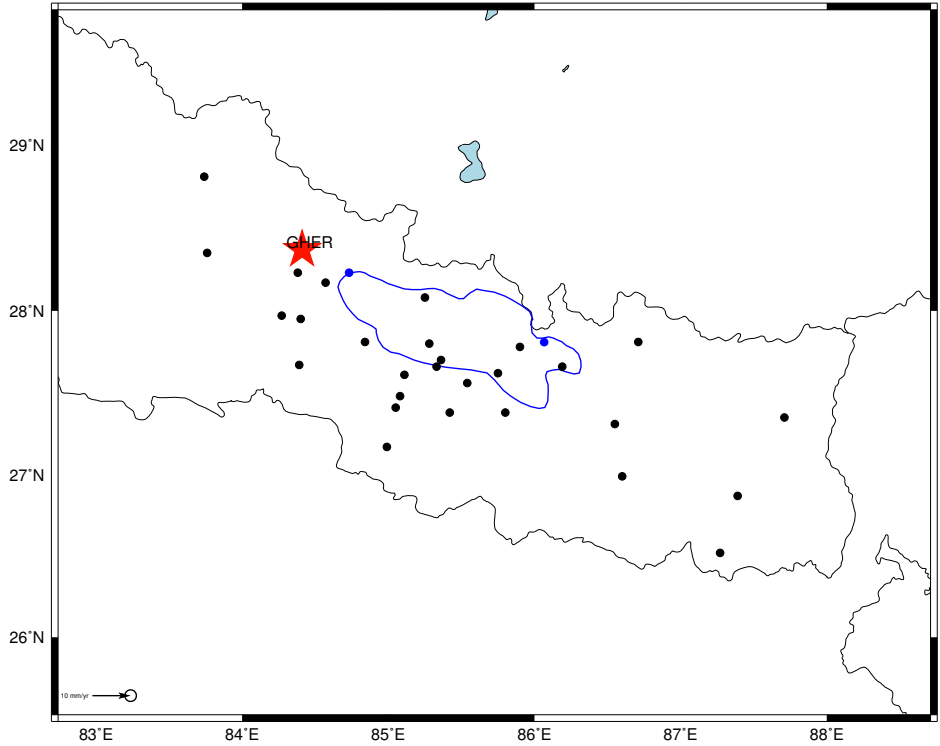
GHER: A=7.6751 D(180)=-7.8267

f(t) = y0 + a exp((1.5 - t) / 43)
a = 7.6751
y0 = -1.9618
R = 0.60287 (lin)

days since EQ

35
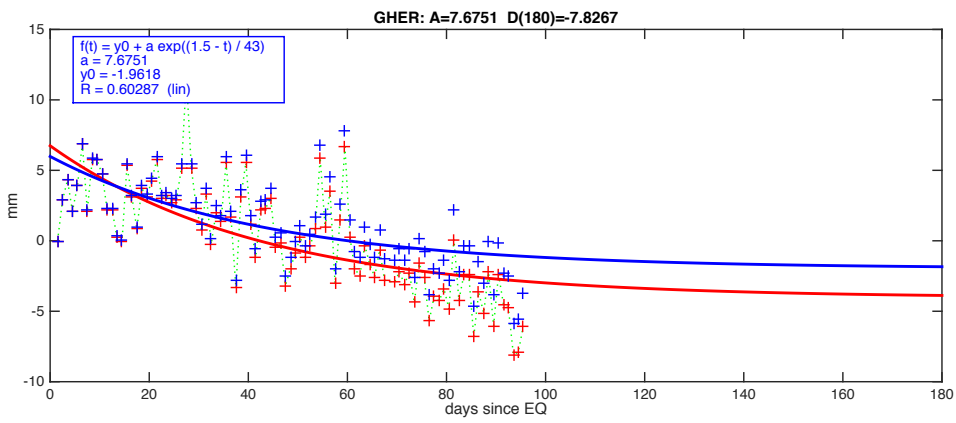
HETA start t=45, end t=180, A=1.8, D_{180}= 5.26 mm
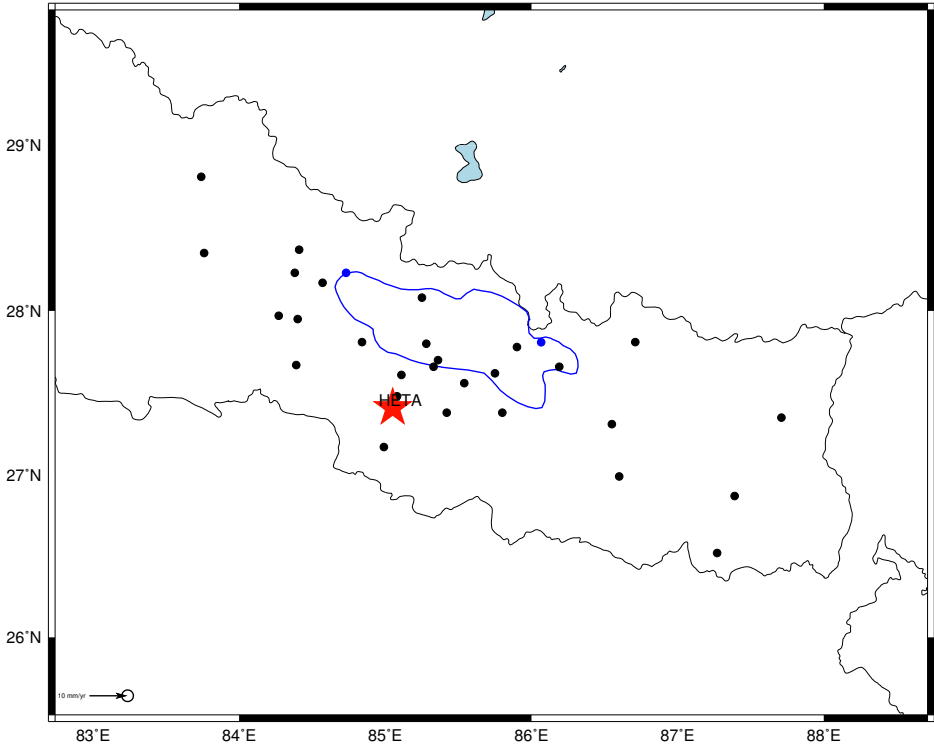
Image produced using p tdefnode.bash:Mencin/Vernant 2015 Version:1.32 Tue Dec 8 11:14:16 MST 2015

HETA: A=1.7709 D(180)=-5.2636

f(t) = y0 + a exp((47.5 - t) / 43)
a = 1.7709
y0 = -1.1744
R = 0.11292 (lin)
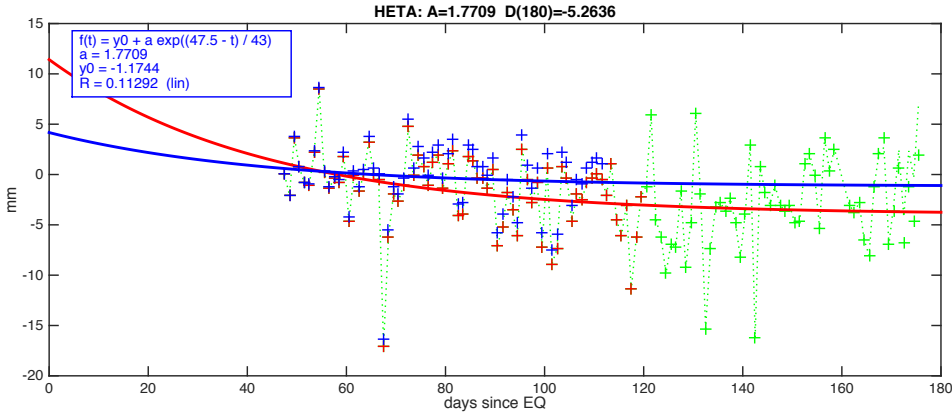
JIR2 start t=24, end t=170, A=14.1, D_{180}= 28.28 mm
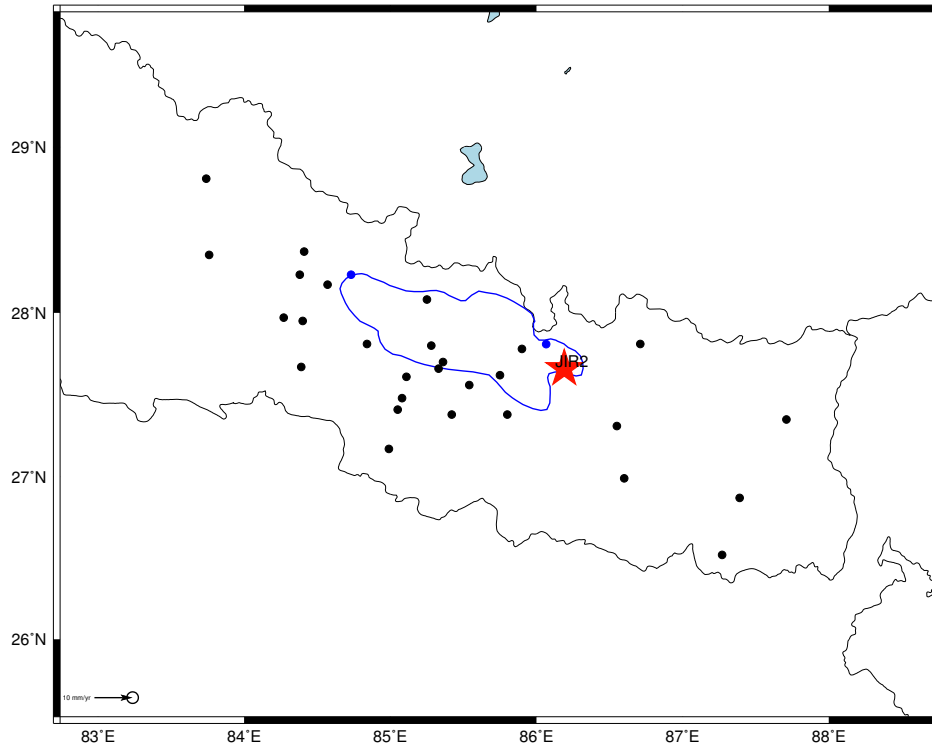
Image produced using p_tdefnode.bash:Mencin/Vernant 2015 Version:1.32 Tue Dec 8 11:14:16 MST 2015

JIR2: A=14.1264 D(180)=-28.2763

f(t) = y0 + a exp((30.5 - t) / 43)
a = 14.126
y0 = -14.342
R = 0.87717 (lin)
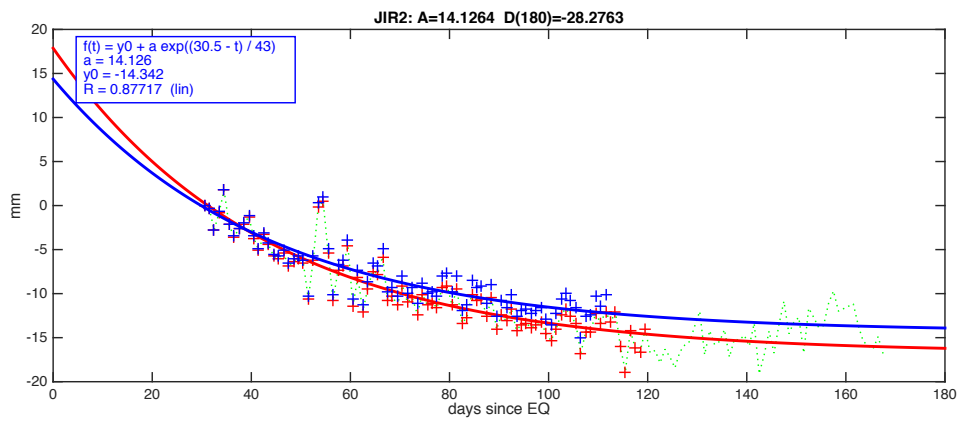
JMSM start t=0, end t=168, A=0.1, D_{180} = 0.13 mm

No significant afterslip
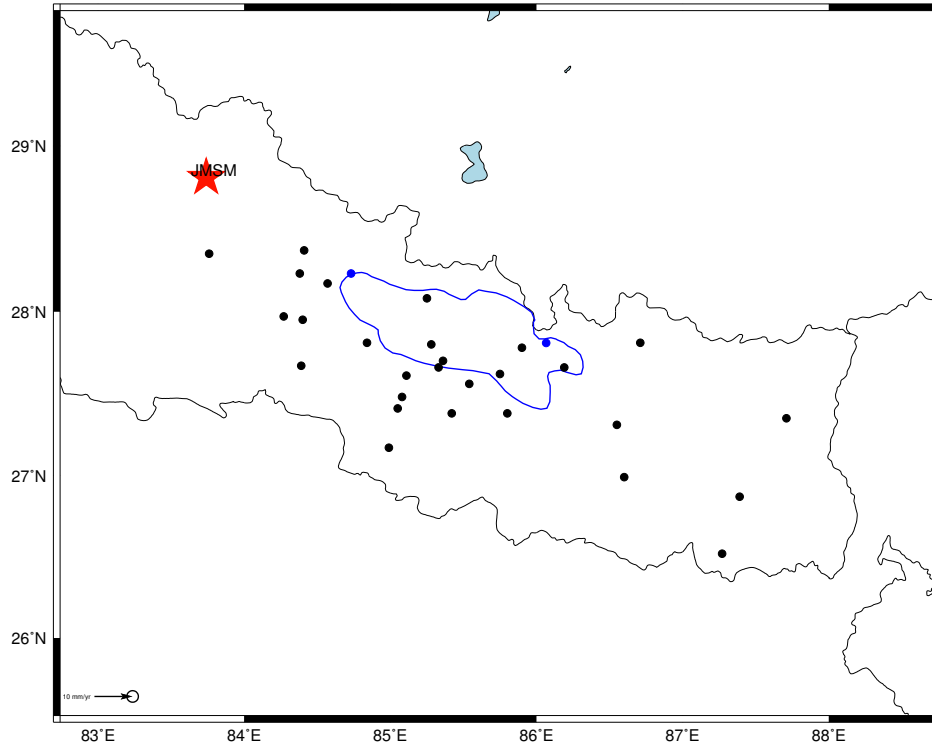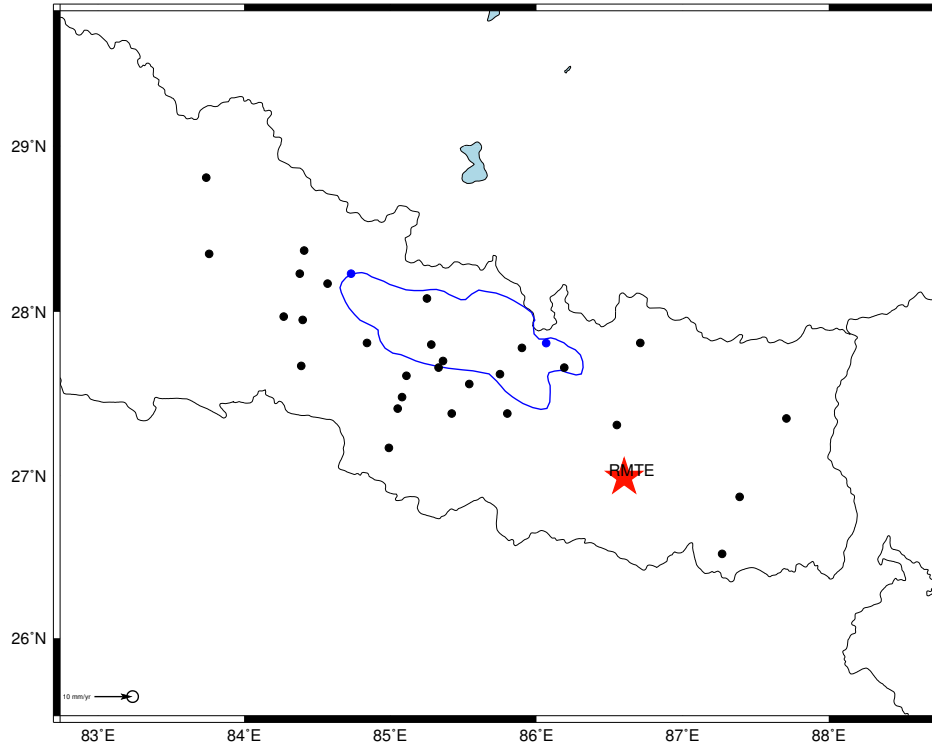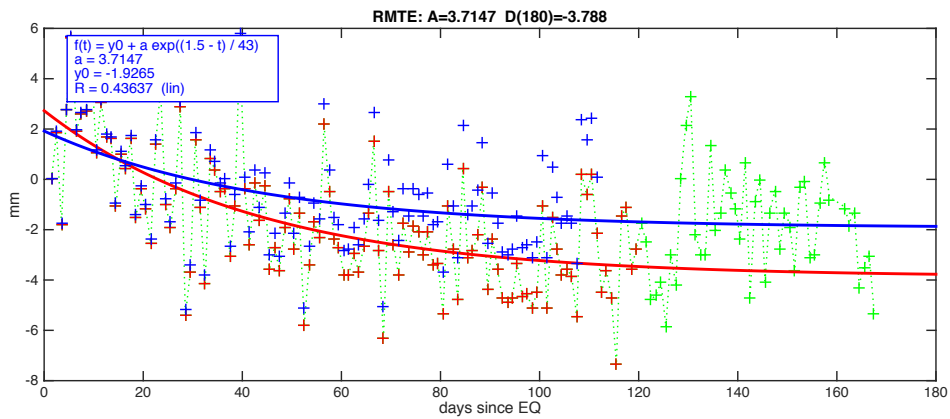

Image produced using p tdefnode.bash:Mencin/Vernant 2015 Version:1.32 Tue Dec 8 11:14:17 MST 2015
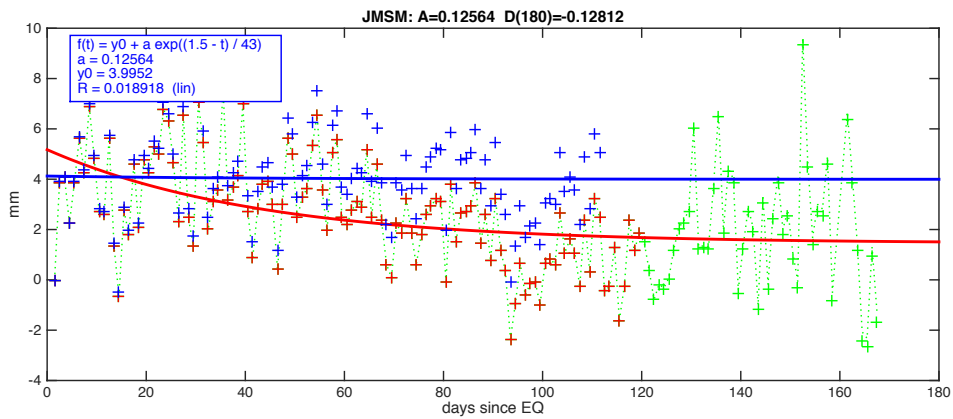
KKN4   t=0 to t=185, A=16.3, D_{180} = 16.61 mm

KKN4 NORTH, interseismic removed

KKN4 NORTH, all signals removed

KKN4 EAST, interseismic removed
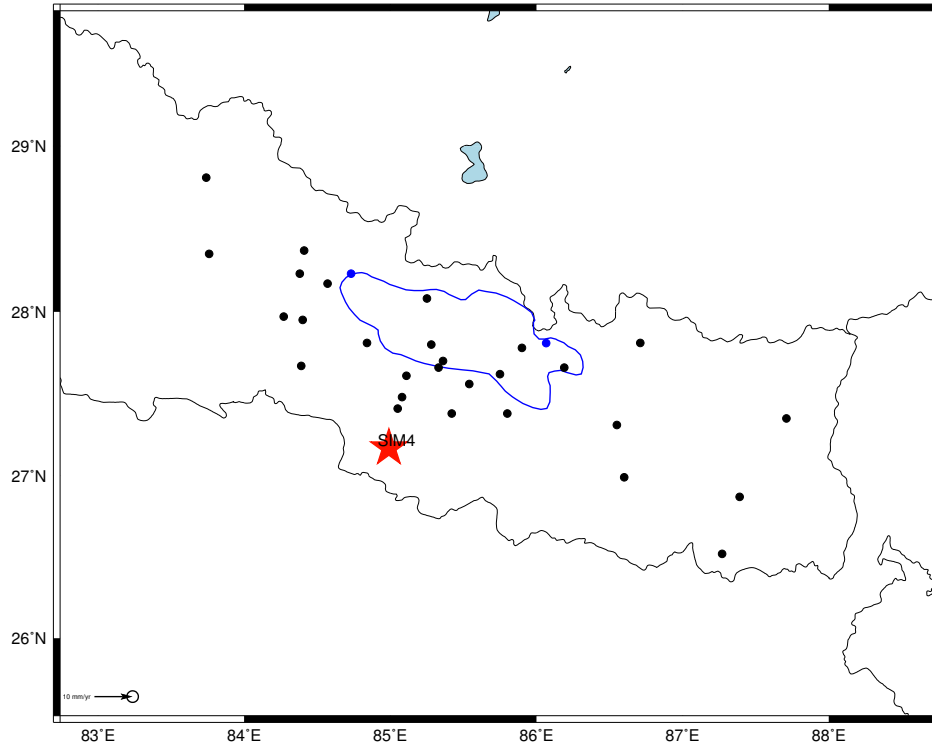
KKN4 EAST, all signals removed
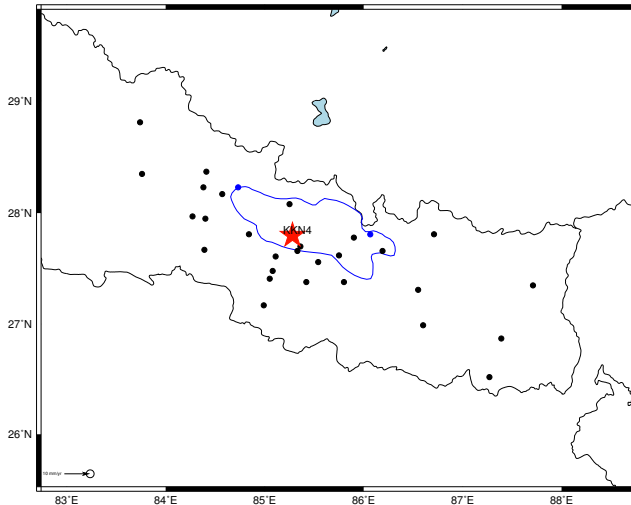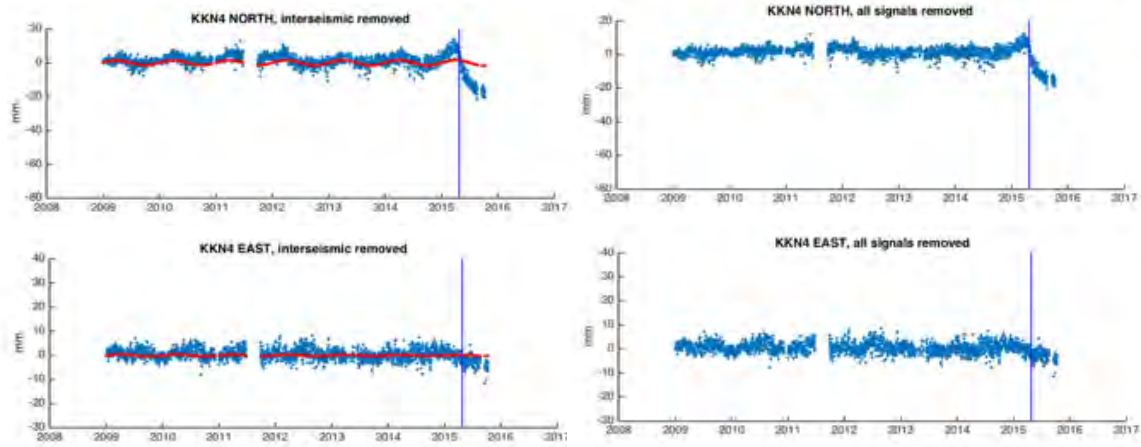
Image produced using p_tdefnode.bash Mencin/Vernant 2015 Version:1.32 Tue Dec 8 11:14:18 MST 2015

KKN4: A=16.287 D(180)=-16.6088

f(t) = y0 + a exp((1.5 - t) / 43)
a = 16.287
y0 = -17.431
R = 0.88739 (lin)

days since EQ
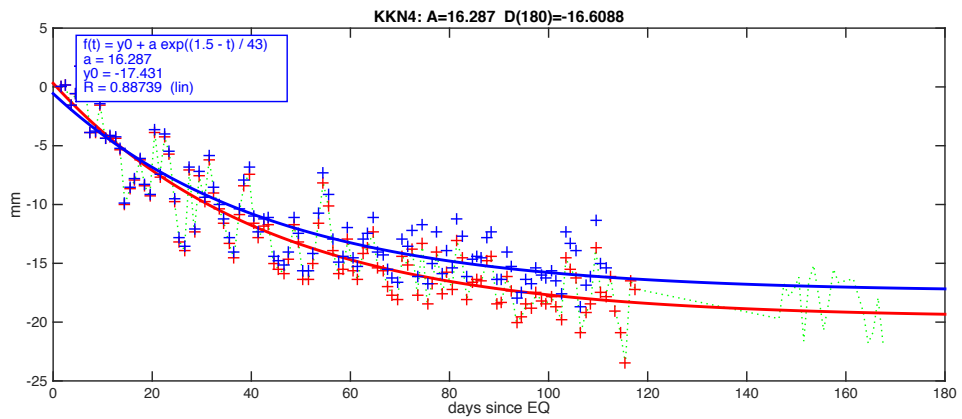
MKLU start t=40, end t=178, ,A=0.77, D_{180}= 1.98 mm

Very sparse data. Fit is artifact.
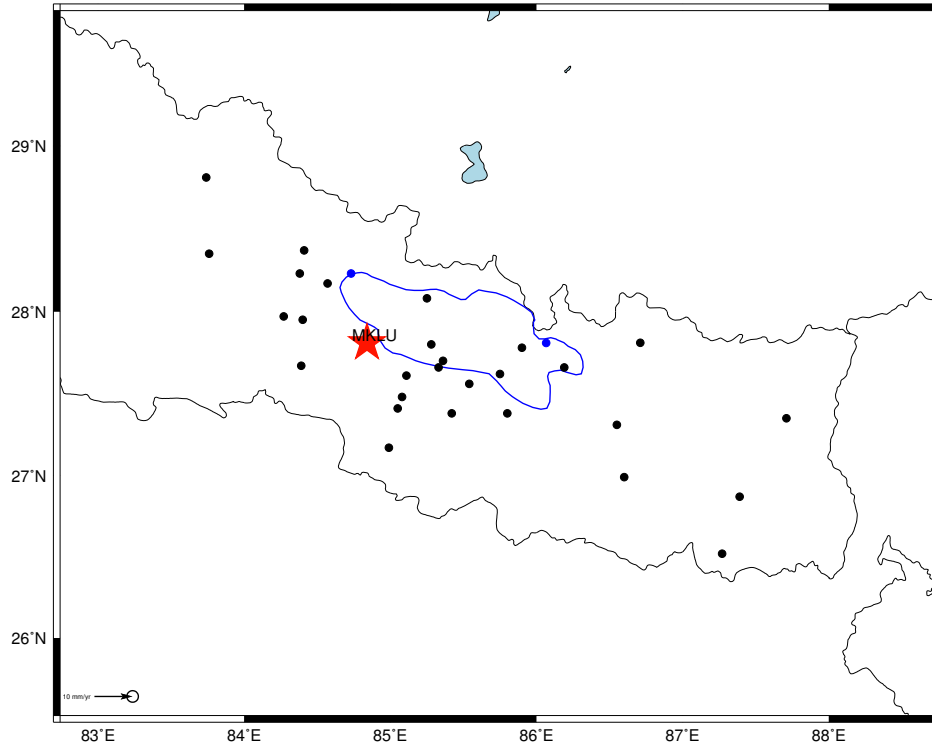
MKLU: A=0.76764 D(180)=-1.9845

f(t) = y0 + a exp((41.5 - t) / 43)
a = 0.76764
y0 = -1.61
R = 0.1999 (lin)

days since EQ

NAST start t=0, end t=178, A=9.2, D_{180}= 9.35
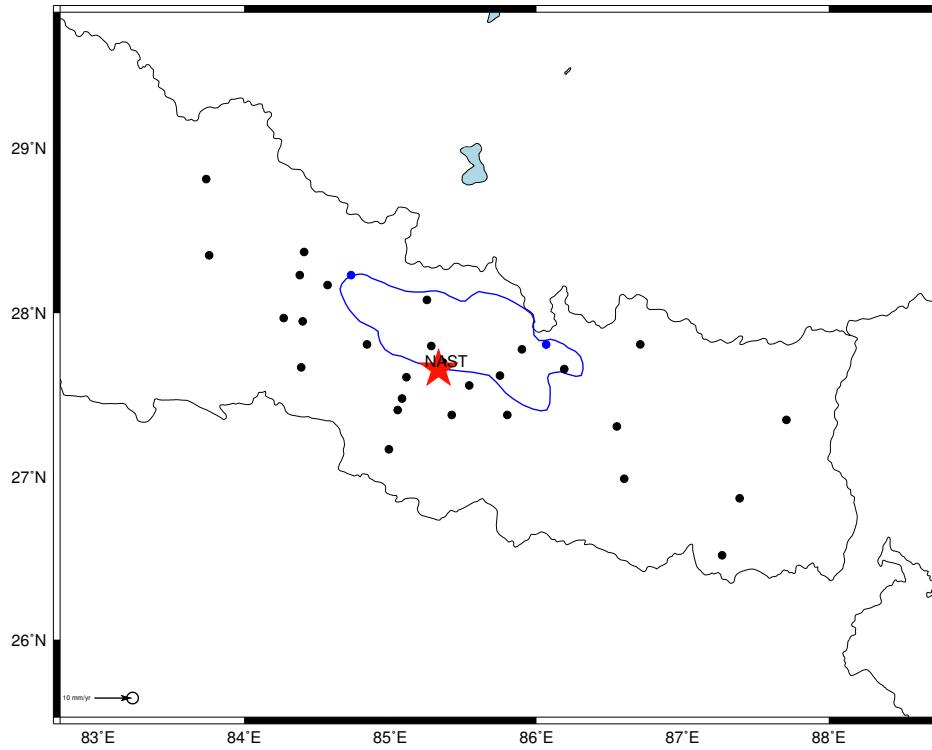
Image produced using p_tdefnode.bash:Mencin/Vernant 2015 Version:1.32 Tue Dec 8 11:14:20 MST 2015

NAST: A=9.1694 D(180)=-9.3506

f(t) = y0 + a exp((1.5 - t) / 43)
a = 9.1694
y0 = -7.1253
R = 0.72967 (lin)
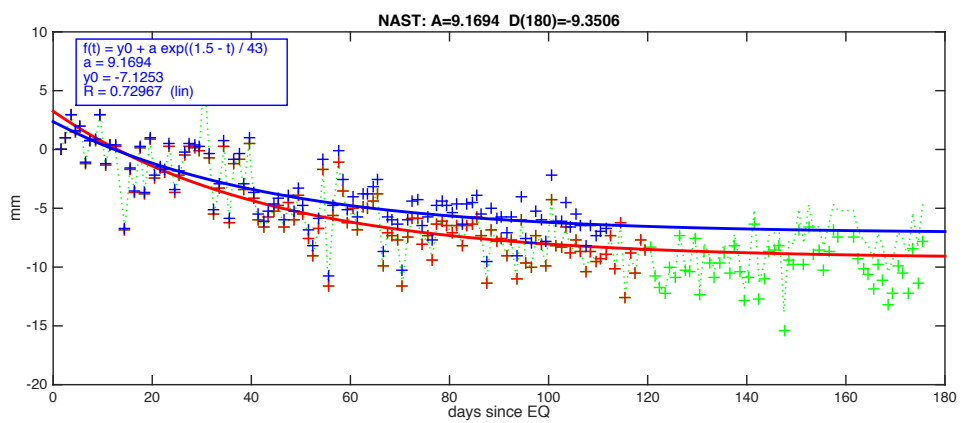
ODRE start t=20, end t=168, No afterslip
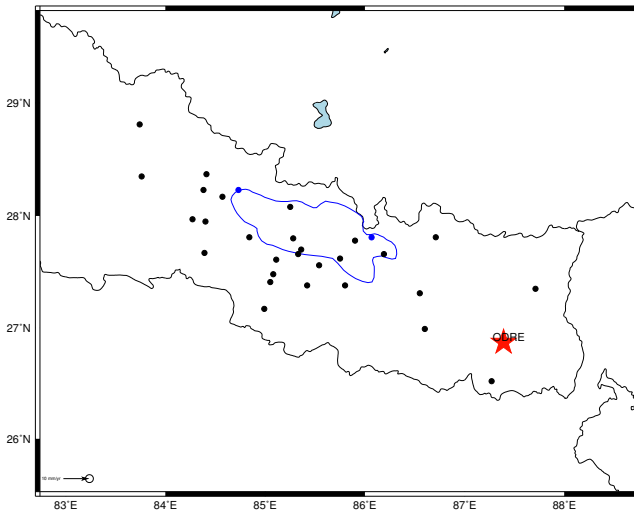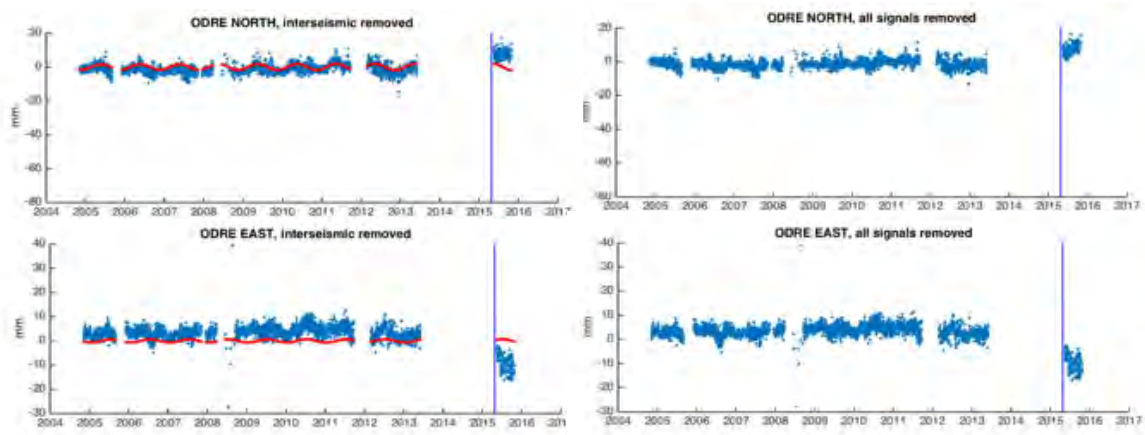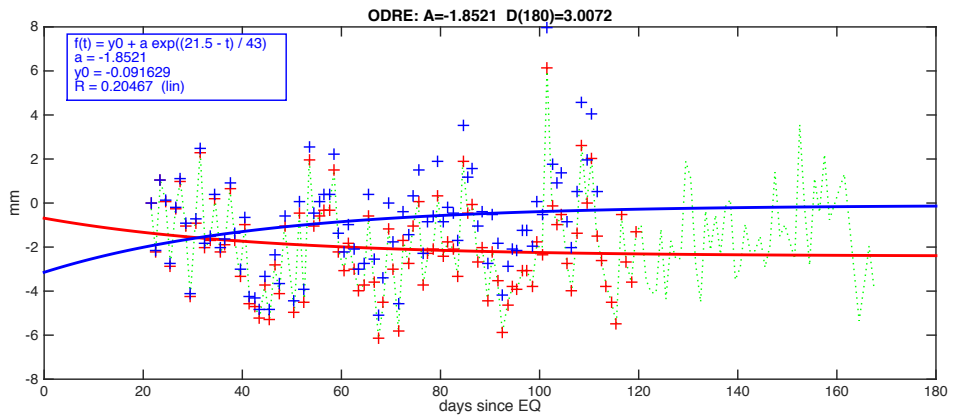
OKR1 start t=20, end t=88, A=1.6, D_{180}= 2.44 mm
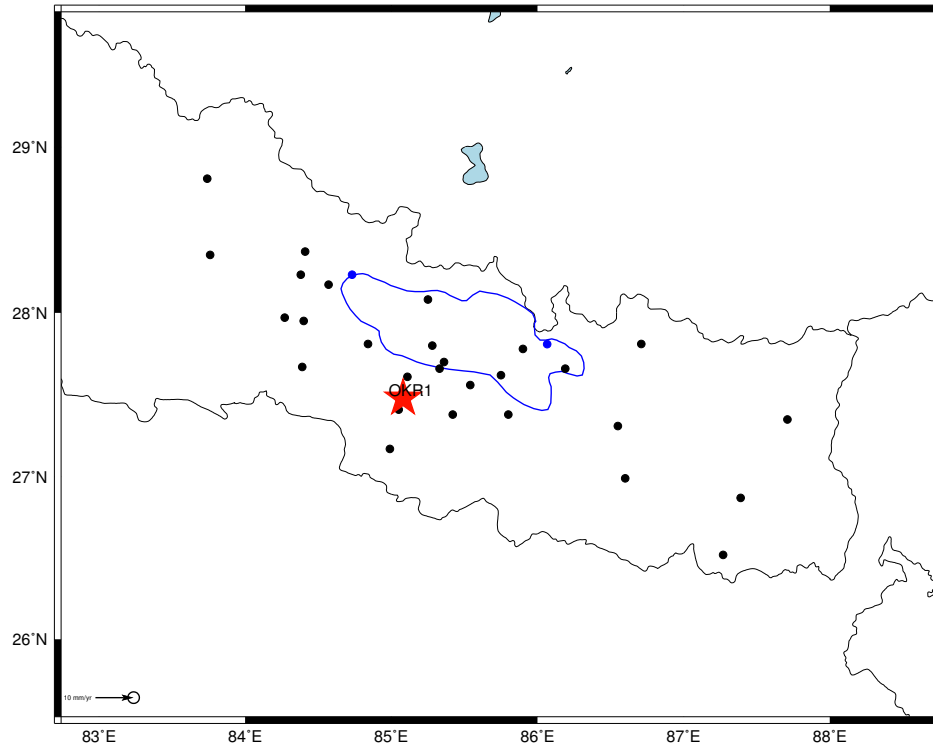
Image produced using p tdefnode.bash:Mencin/Vernant 2015 Version:1.32 Tue Dec 8 11:14:22 MST 2015

OKR1: A=1.5716 D(180)=-2.4358

f(t) = y0 + a exp((19.5 - t) / 43)
a = 1.5716
y0 = 3.1962
R = 0.11296 (lin)
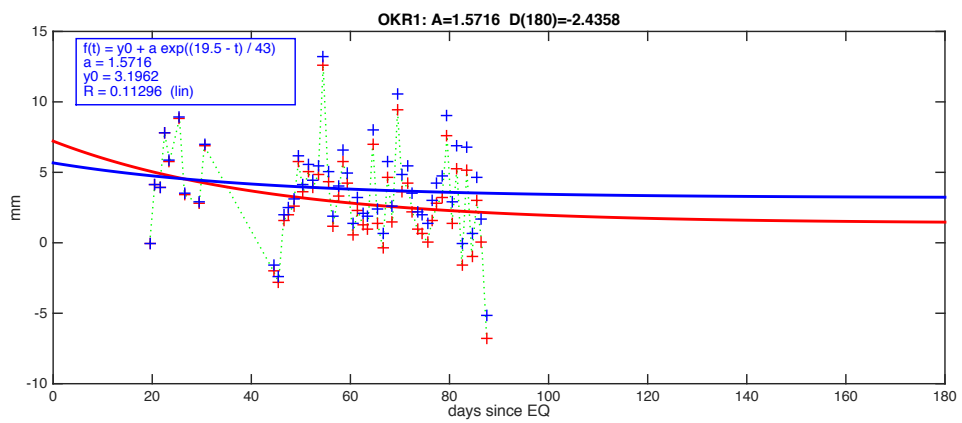
RMJT start t=0, end t=170, A=4.0, D_{180}= 7.38 mm
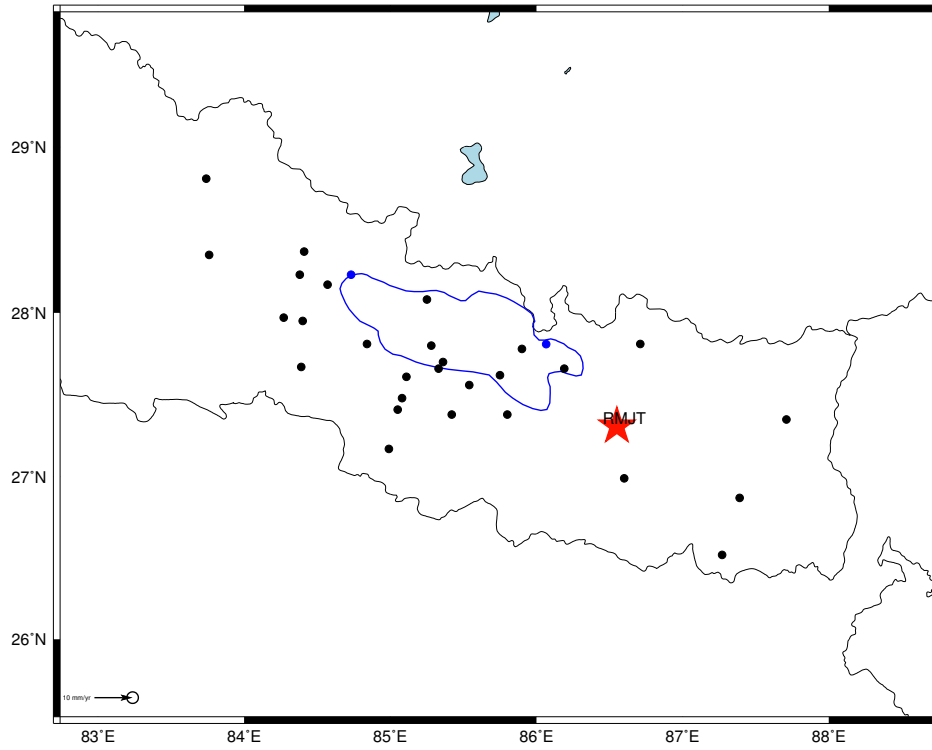
RMJT: A=4.0451 D(180)=-7.3777

f(t) = y0 + a exp((26.5 - t) / 43)
a = 4.0451
y0 = -8.3466
R = 0.43225 (lin)

44
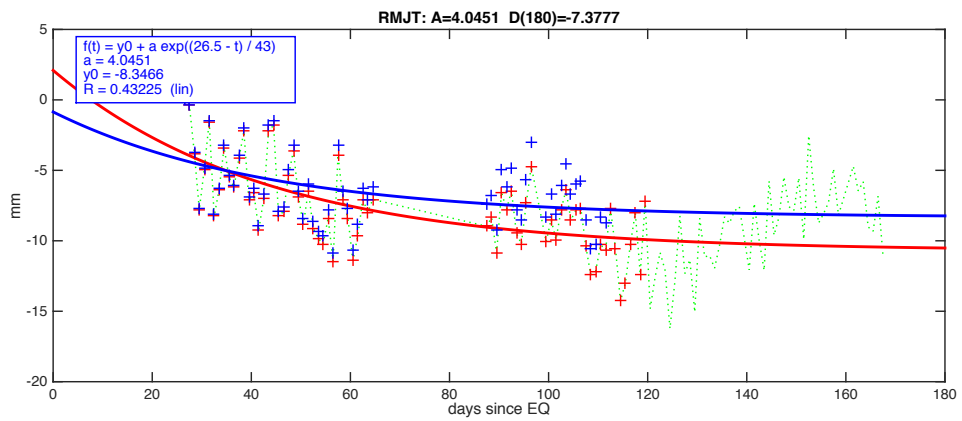
RMTE start t=0, end t=170, A=3.7, D_{180}= 3.79 mm

Image produced using p tdefnode.bash:Mencin/Vernant 2015 Version:1.32 Tue Dec 8 11:14:24 MST 2015

RMTE: A=3.7147 D(180)=-3.788

f(t) = y0 + a exp((1.5 - t) / 43)
a = 3.7147
y0 = -1.9265
R = 0.43637 (lin)

days since EQ

45

SIM4 start t=10, end t=170, A=1.8, D_{180}= 2.30 mm

Image produced using p tdefnode.bash:Mencin/Vernant 2015 Version:1.32 Tue Dec 8 11:14:24 MST 2015

SIM4: A=1.7873 D(180)=-2.2998

f(t) = y0 + a exp((11.5 - t) / 43)
a = 1.7873
y0 = 3.358
R = 0.1981 (lin)
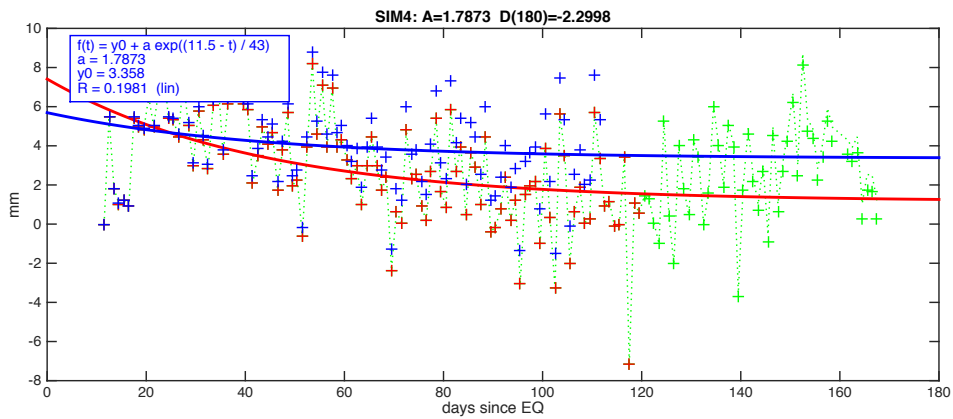
SLBL   start t=38, end t=178, A=4.0, D_{180} = 9.02 mm

SLBL: A=4.0121 D(180)=-9.0212

f(t) = y0 + a exp((35.5 - t) / 43)
a = 4.0121
y0 = -3.8778
R = 0.16872 (lin)
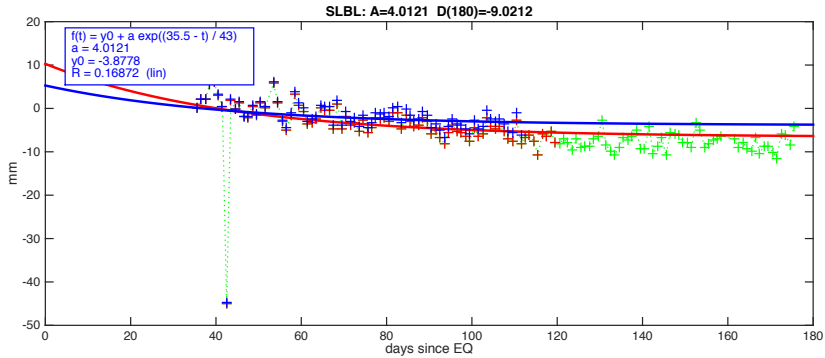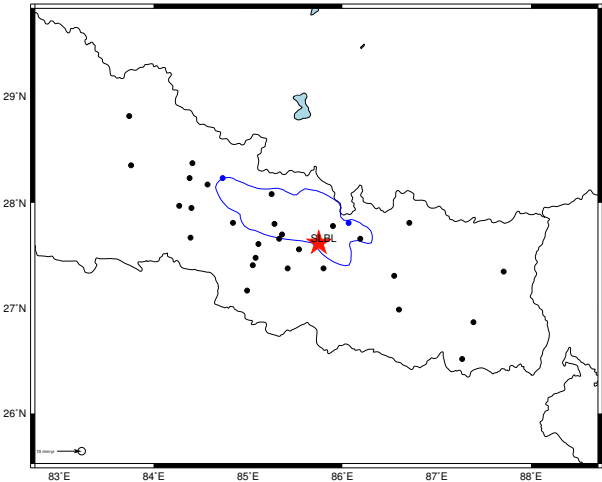
SNDL start t=36, end t=175, A=10.7, D_{180}= 10.90 mm
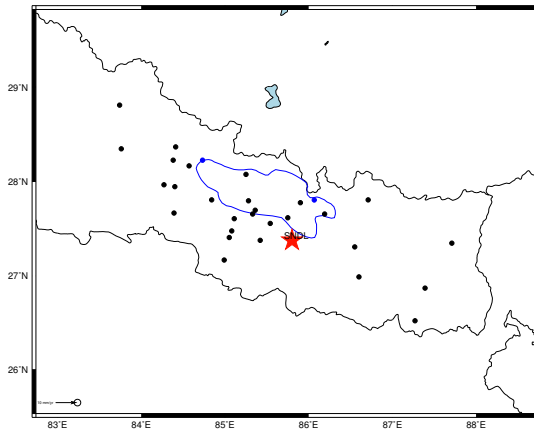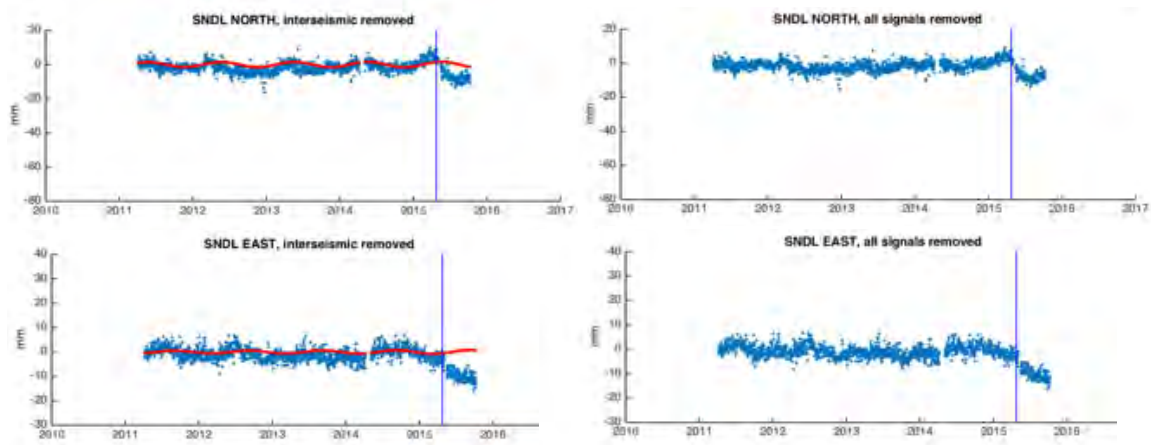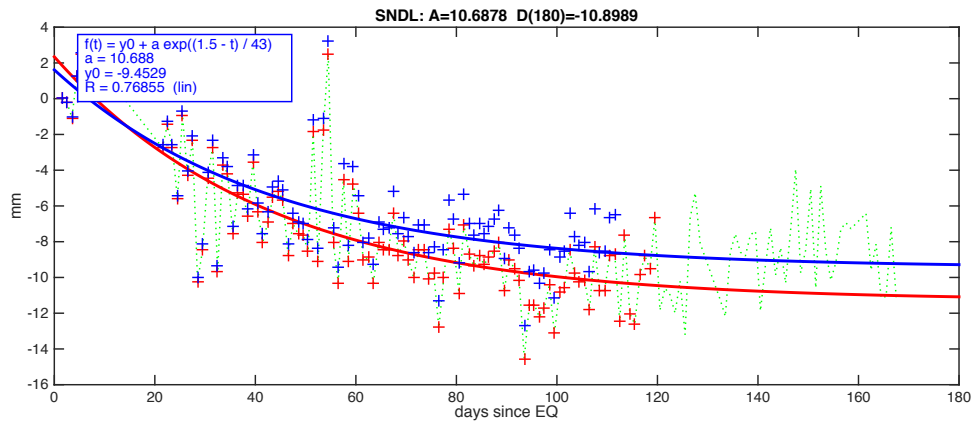
SYBC start t=0, end t=168, A=26.52, D_{180} = 27.15 mm

This site is close to and perturbed by the Mw=7.3 aftershock. Its data are not used.

49
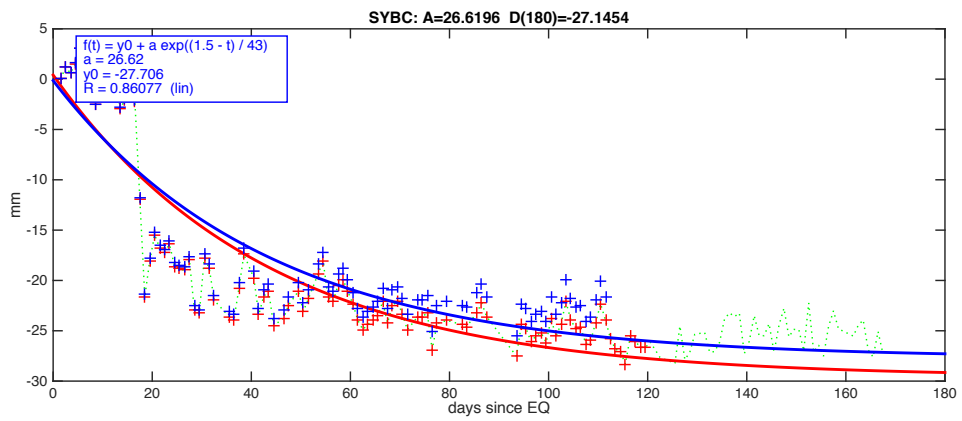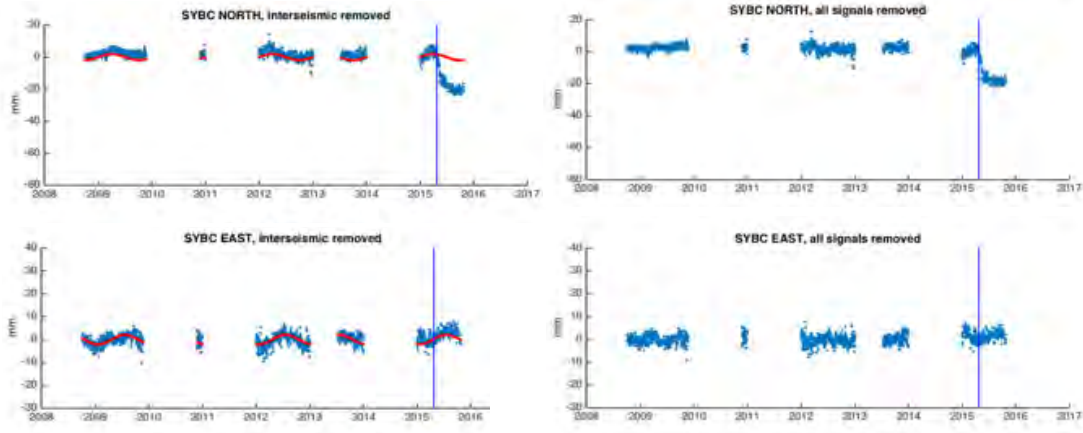
TPLJ start t=0, end t=168, A=3.0, D_{180}= 3.05 mm
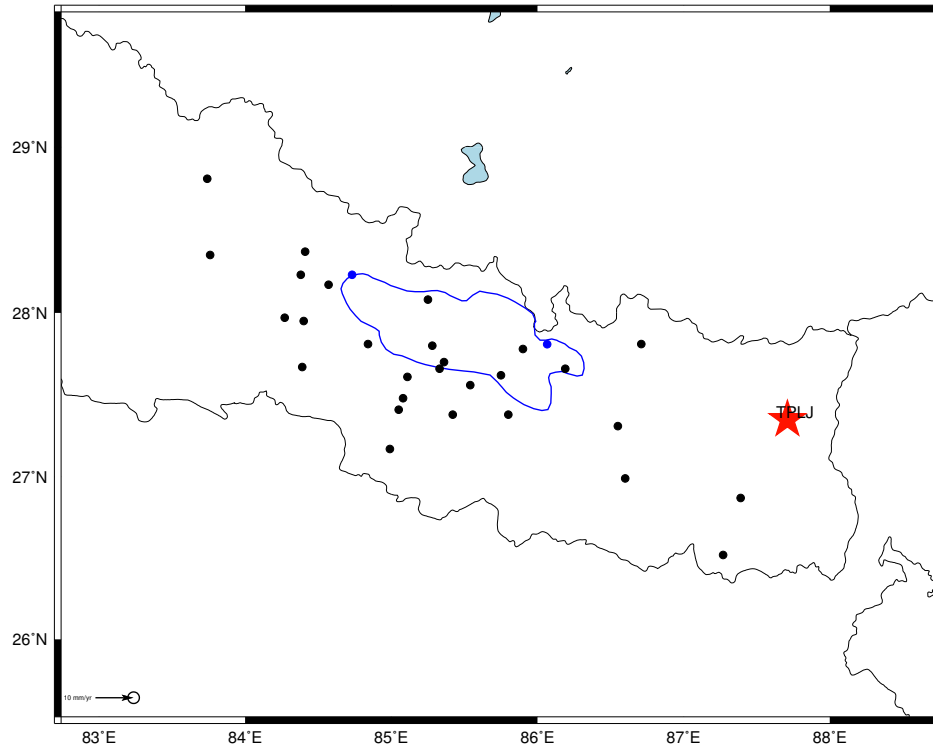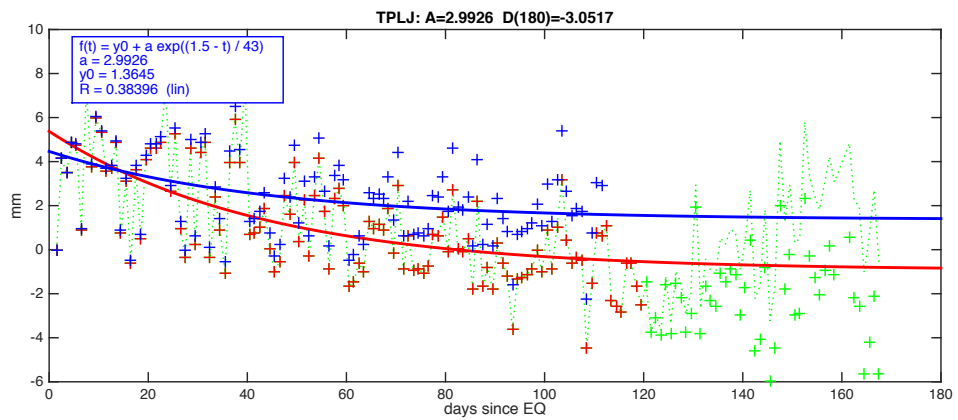

Image produced using p tdefnode.bash:Mencin/Vernant 2015 Version:1.32 Tue Dec 8 11:14:28 MST 2015

TPLJ: A=2.9926 D(180)=-3.0517

$f(t) = y0 + a \exp((1.5 - t) / 43)$
a = 2.9926
y0 = 1.3645
R = 0.38396 (lin)

days since EQ

50

XBAR start t=58, end t=178, A=9.2, D_{180}= 34.33 mm
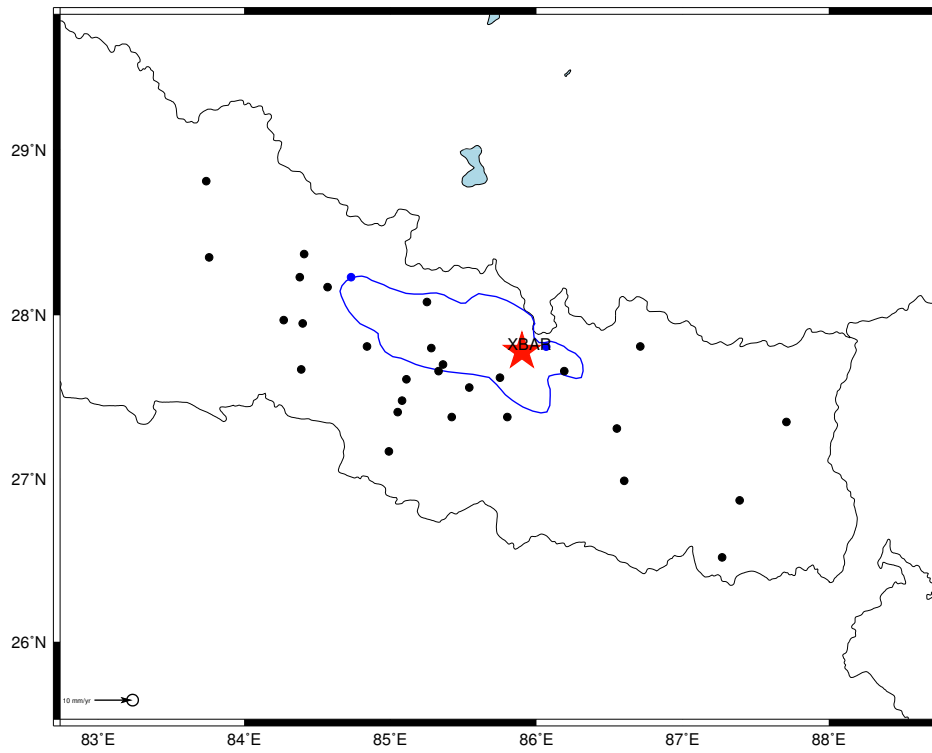
Image produced using p tdefnode.bash:Mencin/Vernant 2015 Version:1.32 Tue Dec 8 11:14:28 MST 2015

XBAR: A=9.1543 D(180)=-34.3332

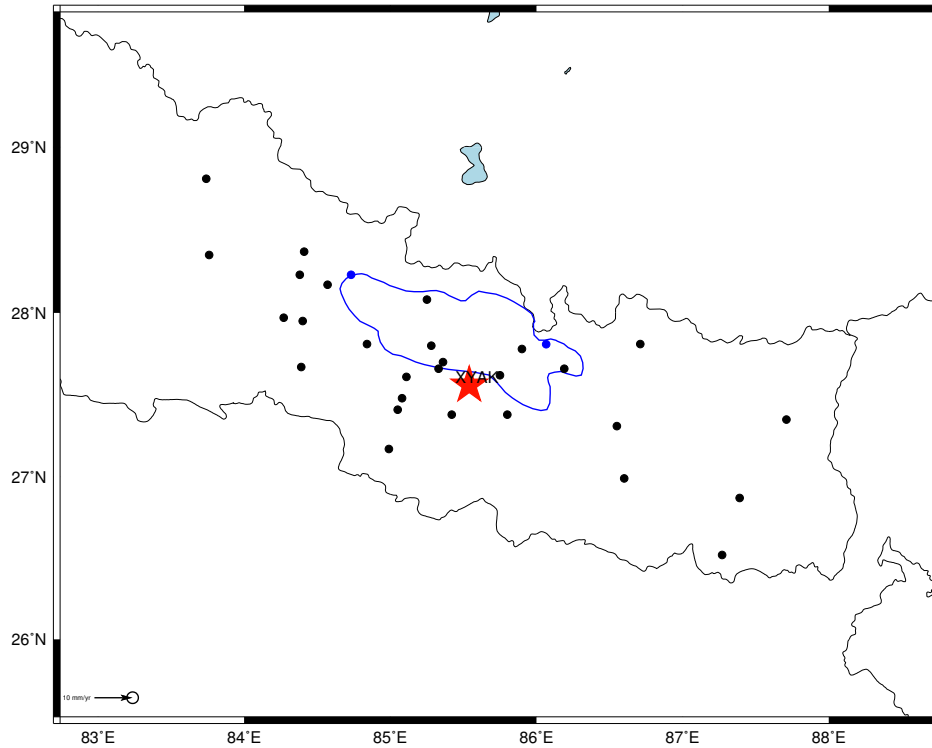f(t) = y0 + a exp((57.5 - t) / 43)
a = 9.1543
y0 = -15.031
R = 0.55858 (lin)

days since EQ

51
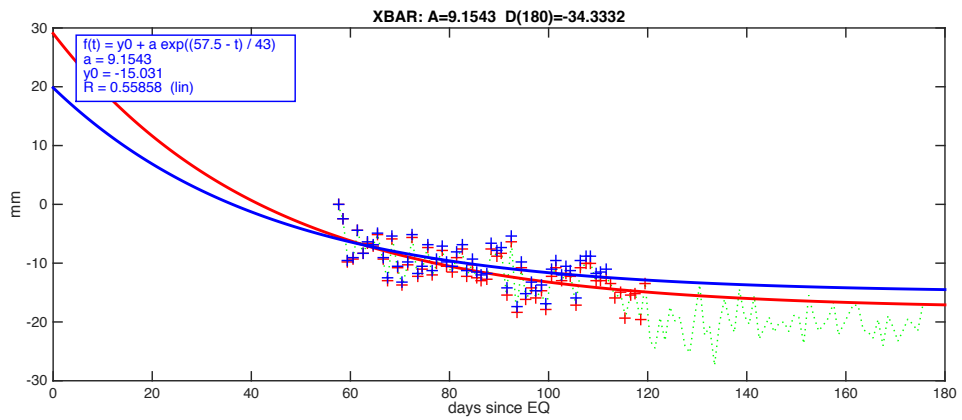
XYAK start t=52, end t=168, A=3.5, D_{180} = 12.23 mm

XYAK: A=3.4967 D(180)=-12.2307

f(t) = y0 + a exp((54.5 - t) / 43)
a = 3.4967
y0 = 0.78661
R = 0.40414 (lin)